Computers and Geotechnics 196 (2026) 108192

Contents lists available at ScienceDirect

Computers and Geotechnics

journal homepage: www.elsevier.com/locate/compgeo

Research paper

Comparison of the three main multifluid extensions of the lattice Boltzmann method used for modeling unsaturated soils

Clara M. Toffoli [a,*], Reihaneh Hosseini [b], Jürgen Grabe [a]

[a] Institute of Geotechnics and Construction Management, Hamburg University of Technology, Hamburg, Germany
[b] Department of Civil and Environmental Engineering, Virginia Tech, Blacksburg, VA, USA

ARTICLE INFO

Keywords:
LBM
Multiphase
Multi-component
Shan–Chen
He–Chen–Zhang
SWRC
Unsaturated soil

ABSTRACT

The complex behavior of unsaturated soils is closely linked to the distribution of the two fluids, water and air, within their pore space. Pore-scale modeling of the fluid distribution can therefore be beneficial for advancing unsaturated soil mechanics. The Lattice Boltzmann Method (LBM) is a popular choice for such modeling, due to its simplicity and computational efficiency. Several extensions of the single-phase LBM have been proposed to model multifluid systems; however, there is no clear consensus on which formulation is most suitable for simulations of unsaturated soils. The objective of this study is to compare the three multifluid approaches commonly used in the field: multiphase Shan–Chen (MPSC), multi-component Shan–Chen (MCSC), and He–Chen–Zhang (HCZ). All three approaches are implemented within an in-house LBM code and are carefully calibrated to ensure consistent interfacial properties. The methods are then applied to simulate drainage and imbibition in a two-dimensional granular packing. Their performance is evaluated in terms of their ability to reproduce pore-scale fluid distributions as well as their computational efficiency. A simple physical model is additionally used to provide qualitative verification of the simulated fluid configurations. The results indicate that, for the capillarity-dominated, quasi-static simulations examined in this study, the MPSC approach provides the most favorable balance between accuracy and computational efficiency.

1. Introduction

The behavior of unsaturated soils is fundamentally more complex than that of saturated soils due to the presence of two interacting fluids, namely water and air, within the pore space. In such soils, key geotechnical properties, including strength, compressibility, and permeability are governed by the distribution of these fluids in the pores and by the pressure difference between them, known as suction, both of which vary with the degree of saturation and hydraulic history. Although the behavior of unsaturated soils can be described empirically based on macroscale experimental observations, more general and predictive frameworks can be developed by gaining a fundamental understanding of the pore-scale mechanisms, particularly fluid distributions, that give rise to the macroscopic response. Numerous experimental studies have pursued this objective using computed tomography (CT) (Schaap et al., 2007; Wang et al., 2023; Kido and Ueda, 2025; Milatz et al., 2022); however, CT imaging is expensive and time consuming, which limits the scope and number of feasible investigations . As an alternative, numerical modeling of pore-scale fluid flow can provide valuable insights into these mechanisms. Among the available pore-scale numerical approaches, the lattice Boltzmann method (LBM) is particularly attractive because it is highly parallelizable, relies on relatively simple equations, can handle complex pore geometries, and offers several well-established multifluid formulations.

Table 1 summarizes the literature on multifluid LBM applied to porous media, including the method used, the problem studies, and key details such as the simulated media and the fluids involved. As shown in the table, Shan–Chen pseudopotential approaches, including the multi-component Shan–Chen (MCSC) and multiphase Shan–Chen (MPSC) formulations, are the most widely used, likely due to their relative simplicity compared to other methods. In the multi-component formulation, the two fluids are modeled as separate components, whereas in the multiphase formulation, they are treated as different phases of the same fluid linked through an equation of state. Among these two approaches, MCSC has been used more frequently, despite its more complex formulation and higher computational cost. This preference likely arose because the application of multifluid LBM to porous media historically originated in petroleum engineering, where the fluids of interest were typically water and oil and were therefore naturally treated as distinct components, making the MCSC formulation a more intuitive choice. As LBM was later adopted for studies of unsaturated

* Corresponding author.
E-mail address: clara.toffoli@tuhh.de (C.M. Toffoli).

https://doi.org/10.1016/j.compgeo.2026.108192
Received 12 January 2026; Received in revised form 20 April 2026; Accepted 22 April 2026
Available online 27 April 2026

Table 1
Summary of the literature on multifluid LBM applications in porous media. MCSC: multi-component Shan–Chen; MPSC: multiphase Shan–Chen; HCZ: He–Chen–Zhang; CG: color-gradient.

Method	Author (Year)	Topic	Simulated media	Fluids involved
MCSC	Pan et al. (2004)	Drainage–imbibition	Tubes, 3D porous media	Tetrachloroethylene–water
MCSC	Schaap et al. (2007)	Flow, CT	3D porous media	Air–water, Soltrol–water
MCSC	Sukop et al. (2008)	Oil invasion, CT	3D porous media	Oil–water
MCSC	Galindo-Torres et al. (2016)	Drainage and imbibition	3D porous media	Unspecified
MCSC	Li et al. (2018)	Two-phase flow	2D porous media	Oil–water, NAPL–water
MCSC	Nekoeian et al. (2018)	Flow, CT	2D porous media	Oil–water
MCSC	Montellà et al. (2020)	Pore invasion modeling	Droplet, tubes, 2 particles	Unspecified, immiscible
MCSC	Zhou et al. (2020)	Oil recovery: flow	2D porous media	Acidic fluid–oil
MCSC	Zhao et al. (2021)	Contact angle	Fluids + wall	Alkanes–water
MPSC	Sukop and Or (2004)	Drainage–imbibition, flow	2D porous media	Air–water
MPSC	Delenne et al. (2015)	Liquid clusters statistics	2D porous media	Air–water
MPSC	Khajepor et al. (2019)	Flow - boundary conditions	Fluids + wall	Air–water
MPSC	Benseghier et al. (2022)	Droplet and menisci	1 or 2 particles	Air–water
MPSC	Hosseini et al. (2024)	Drainage–imbibition hysteresis	2 and 3D porous media	Air–water
HCZ	Yiotis et al. (2007)	Flow, permeability	2D porous media	Unspecified, immiscible
HCZ	Fakhari et al. (2018)	Flow, imbibition	2D porous media	CO_2-water
HCZ	He et al. (2019)	Solid–fluids interaction	One to three particles	Air–water
HCZ	Wang and Peng (2020)	Boundary conditions	2D porous media	Unspecified, immiscible
HCZ	Younes et al. (2022)	Liquid bridges and coalescence	1 to 3 particles	Air–water
CG	Liu et al. (2015)	CO_2 sequestration	2D porous media	CO_2-water

soils, use of the MPSC formulation increased, possibly motivated by the ability of multiphase formulations to represent phase transitions such as evaporation and condensation, which were not possible in multi-component formulations (Sukop and Or, 2004), as well as by their lower computational cost compared to MCSC. However, more recent studies suggest that the MPSC formulation is not thermodynamically consistent at temperatures relevant to unsaturated soils (Younes et al., 2023) and consequently adopt the He–Chen–Zhang (HCZ) method as an alternative multiphase approach. Other formulations, including the color-gradient (CG) and free-energy (FE) methods, have seen limited application in porous media studies. In this work, the abbreviations MPSC, MCSC, and HCZ are used consistently to denote the multiphase Shan–Chen, multicomponent Shan–Chen, and He–Chen–Zhang formulations, respectively, noting that terminology for these models can vary across the LBM literature.

Given the various multifluid LBM formulations used in the study of porous media, an important question is which approach is most suitable for investigating the behavior of unsaturated soils.[1] A suitable method must accurately capture the fluid distribution of air and water and the suction between those phases while remaining computationally efficient enough to allow simulations of representative sample sizes. The air–water system in unsaturated soils may be interpreted both as multiphase (water and water vapor) and as multi-component (water and other gases in air). As a result, it remains unclear whether a multi-component or a multiphase formulation provides a more representative description of unsaturated soil behavior, and, if a multiphase approach is adopted, whether the thermodynamic consistency of formulations such as HCZ plays a critical role. Most studies summarized in Table 1 do not explicitly justify their choice of multifluid LBM formulation. Some studies have attempted to compare different multifluid LBM formulations by performing similar simulations using multiple methods; however, these comparisons have primarily focused on numerical capabilities through simplified benchmark problems, such as single-droplet tests or Poiseuille flow of binary fluids, rather than on comparisons of fluid distributions within granular packings. For example, Ye et al. (2018) compared MPSC and HCZ in terms of achievable contact-angle ranges and magnitude of spurious currents, while Yang and Boek (2013) compared MPSC, CG, and FE formulations based on the ranges of density and viscosity ratios they can accommodate. Liu et al. (2016) presented a review that similarly emphasized numerical capabilities and stable operating ranges. Nevertheless, an open question remains: when contact angle, density ratio, and viscosity ratio fall within the stable operating range of all formulations, does one method consistently outperform the others in simulating fluid distributions in granular media, and, if so, does this improved performance justify the associated computational cost? Answering this question would determine whether a particular formulation should be preferred for future studies of unsaturated soils.

Accordingly, the objective of this paper is to compare these three commonly used multifluid LBM formulations (MCSC, MPSC, and HCZ) in terms of their ability to capture fluid distributions and suction in unsaturated granular soils under equilibrium conditions. The goal is not to provide a universal ranking of multifluid LBM methods, but rather to evaluate their relative performance under the specific conditions relevant to capillarity-dominated, quasi-static processes in unsaturated soils. To achieve this objective, a drainage and imbibition cycle is simulated in a two-dimensional (2D) granular packing using each formulation, with all simulations performed using in-house developed code. Although the code is capable of simulating three-dimensional (3D) media, a 2D configuration is adopted here because 2D simulations can reproduce pore-emptying and pore-filling mechanisms similar to those observed in 3D systems (Hosseini et al., 2024), while offering improved visualization of pore-scale processes and substantially reduced computational cost. Comparisons of fluid distributions are conducted

[1] LBM alone is not sufficient to model the behavior of unsaturated soils and must be coupled with the discrete element method (DEM) to simulate interactions between moving soil grains (Younes et al., 2023); however, the first step is the selection of an appropriate LBM formulation capable of producing the correct capillary forces for transfer to DEM (Hosseini and Kumar, 2025).

through qualitative visualization of simulations at comparable stages of the drainage–imbibition cycle. In addition, the formulations are evaluated quantitatively using the suction and saturation values obtained during the simulations and the resulting soil–water retention curve (SWRC), a widely used descriptor of unsaturated soil behavior.

The remainder of the paper is organized as follows. Section 2 summarizes the formulation of each multifluid LBM approach considered. Section 3 describes the calibration of each method, in terms of surface tension and contact angle, to ensure that the same physical process is modeled across the three formulations. Section 4 details the simulation setup, while Section 5 describes the physical model used for qualitative validation. Finally, Section 6 presents the results and provides a detailed discussion of the comparisons.

2. Numerical methods

This section first provides a summary of the basic principles of LBM, followed by descriptions of the three multifluid formulations employed in this study, highlighting their key differences. A comparative summary of these formulations is provided at the end of the section in Table 2. Please consult the nomenclature for the definition of each variable.

2.1. Basics of the lattice Boltzmann method

In the LBM framework, a particle distribution function (PDF) $f_i(\mathbf{x},t)$ is introduced to represent the particle population within a discrete lattice (Huang et al., 2015). $f_i(\mathbf{x},t)$ evolves based on the discretized Boltzmann transport equation, shown in Eq. (1). The discretization in this context is done in space and in time. In space, a lattice is established, in which each node communicates with predefined neighboring nodes according to the lattice velocities e_i. With respect to time, the discretization is defined by the time step Δt. The discrete velocity model is described by its dimensions and also by the number of nodes each node communicates with, represented by DxQy, in which x represents the dimensions and y is the number of communicating nodes. In this study, D3Q19 (Qian et al., 1992; Martys and Chen, 1996) is used for all simulations, meaning that the simulations are 3 dimensional and each lattice node can stream to 19 other nodes, including itself.

Each time step consists of two substeps: collision and streaming. During the collision step, the current distribution function $f_i(\mathbf{x},t)$ is relaxed toward the equilibrium state $f_i^{eq}(\mathbf{x},t)$ calculated based on the Maxwell–Boltzmann distribution function as indicated in Eq. (2) (Krüger, 2017). The velocity used in this equation is the equilibrium velocity, which might or might not coincide with the macroscopic velocity of the fluid, depending on the method as discussed below. This relaxation process is represented by the right-hand side of Eq. (1). The subsequent streaming step involves propagating the post-collision distribution functions to neighboring lattice nodes along discrete velocity directions $\mathbf{e_i}$.

$$f_i\left(\mathbf{x}+\mathbf{e_i}\Delta t, t+\Delta t\right) = f_i(\mathbf{x},t) - \frac{1}{\tau}\left(f_i(\mathbf{x},t) - f_i^{eq}(\mathbf{x},t)\right) + S_i(\mathbf{x},t) \tag{1}$$

$$f_i^{eq}(\mathbf{x},t) = w_i\rho\left[1 + \frac{\mathbf{e_i}\cdot\mathbf{u}}{c_s^2} + \frac{(\mathbf{e_i}\cdot\mathbf{u})^2}{2c_s^4} - \frac{\mathbf{u}^2}{2c_s^2}\right] \tag{2}$$

The zeroth and first moments of $f_i(\mathbf{x},t)$ yield the macroscopic fluid density and velocity, respectively, as presented in Eqs. (3) and (4). It should be noted that the expression for the velocity may differ if an external force is applied or if an alternative forcing scheme is employed, as discussed in the following subsections.

$$\rho(\mathbf{x},t) = \sum_i f_i(\mathbf{x},t) \tag{3}$$

$$\rho\mathbf{u}(\mathbf{x},t) = \sum_i \mathbf{e}_i f_i(\mathbf{x},t) \tag{4}$$

Additional general LBM settings in this study include using the Bhatnagar–Gross–Krook (BGK) collision operator (Luo et al., 2011) and enforcing a no-slip boundary condition at solid–fluid interfaces through the bounce-back scheme (Ginzbourg and Adler, 1994).

2.2. Multiphase Shan–Chen (MPSC)

In the MPSC formulation (Shan and Chen, 1993), a single fluid component, represented by one PDF, is divided into two phases by the so-called inter-particle force, according to Eq. (5). The interaction strength is controlled by the parameter G in the equation. $\psi(\mathbf{x},t)$ represents the mean-field potential, a function of density.

$$\mathbf{F_{int}}(\mathbf{x},t) = -G\psi(\mathbf{x},t)\sum_i w_i\psi\left(\mathbf{x}+\mathbf{e_i}\Delta t,t\right)\mathbf{e}_i \tag{5}$$

The simplest forcing scheme for the MPSC extension is that proposed by Shan and Chen (1993). In this formulation Eq. (1) contains no explicit source term, and the macroscopic velocity is computed using Eq. (6), where $\mathbf{F}$ represents the sum of inter-particle and any external forces.

$$\mathbf{u^{eq}} = \frac{1}{\rho}\sum_i f_i\mathbf{e_i} + \frac{\mathbf{F}\tau}{\rho} \tag{6}$$

To determine the system pressure, an equation of state (EoS) must be specified. To enhance achievable density ratios and reduce spurious currents, the Carnahan–Starling EoS (Carnahan and Starling, 1969), presented in Eq. (7), is adopted for the multiphase simulations, according to the procedure and suggestions of Yuan and Schaefer (2006). Based on the values of the parameters a and b in the EoS, a critical temperature T_c can be determined, above which phase separation does not occur. Therefore, the temperature T in the simulations should be set below T_c. Refer to Hosseini et al. (2024) for more details.

$$p = \rho RT\frac{1+b\rho/4+(b\rho/4)^2-(b\rho/4)^3}{(1-b\rho/4)^3} - a\rho^2 \tag{7}$$

2.3. Multi-component Shan–Chen (MCSC)

In the MCSC formulation (Martys and Chen, 1996; Shan and Doolen, 1995), two fluid components coexist without undergoing phase separation and are tracked by their own PDF. In the equations below, the index σ indicates each one of these components. Depending on the selected parameters, the components may be miscible or immiscible. Their mutual interaction, representing fluid–fluid cohesion, is governed by the parameter $G_{\sigma\bar{\sigma}}$ in Eq. (8), which defines the cohesive force between components. This parameter also controls the thickness of the interface in case of immiscible fluids: larger values of $G_{\sigma\bar{\sigma}}$ produce stronger repulsion and thus thinner interfaces. The value of the parameter is imposed for each fluid pair, where higher positive values correspond to stronger repulsion and thus immiscibility, while small positive values lead to attraction and thus miscibility. Negative values are not physically meaningful in this context.

$$\mathbf{F}_{\mathbf{c},\sigma}(\mathbf{x},t) = -G_{\sigma\bar{\sigma}}\rho_\sigma(\mathbf{x},t)\sum_i w_i\rho_{\bar{\sigma}}(\mathbf{x}+\mathbf{e}_i\Delta t,t)\mathbf{e}_i \tag{8}$$

The interaction between fluid and nearby solids is introduced through a fluid–solid adhesion force, defined in Eq. (9). The parameter $G_{ads,\sigma}$ determines the strength of this interaction and thereby controls the contact angle between the fluids and the solid in the simulations.

$$\mathbf{F_{ads},\sigma}(\mathbf{x},t) = -G_{ads,\sigma}\rho_\sigma(\mathbf{x},t)\sum_i w_i s\left(\mathbf{x}+\mathbf{e}_i\Delta t,t\right)\mathbf{e}_i \tag{9}$$

Because this method involves multiple components, each fluid node in the computational domain contains a density contribution from each component. These are referred to as main and dissolved or dissolved associated densities by Huang et al. (2007) and Zhao et al. (2021) and others. The sum of the main and dissolved densities remains approximately constant throughout the domain (Huang et al., 2007),

corresponding to the initially prescribed total density. As a result, the method is best suited for systems with components of comparable densities, such as water and oil.

Equations for velocity and pressure are then required. The chosen forcing scheme for the MCSC extension is once again the Shan and Chen one (Shan and Chen, 1993). Consequently, Eq. (1) does not include an explicit source term, and the macroscopic velocity is computed using Eq. (10), where $\mathbf{u}'$ represents the common averaged velocity of the two fluid components without considering forces, as defined in Eq. (11). The macroscopic pressure is obtained from Eq. (12) (Huang et al., 2015), and the resulting value applies for both components.

$$\mathbf{u}_{\sigma}^{eq} = \mathbf{u}' + \frac{\tau^{\sigma}\mathbf{F}_{\sigma}}{\rho_{\sigma}}, \tag{10}$$

$$\mathbf{u}' = \sum_{\sigma=1}^{2} \frac{\rho_{\sigma}\mathbf{u}_{\sigma}}{\tau^{\sigma}} \Big/ \sum_{\sigma=1}^{2} \frac{\rho_{\sigma}}{\tau^{\sigma}}, \tag{11}$$

$$p = c_s^2(\rho_{\sigma} + \rho_{\bar{\sigma}}) + c_s^2 G_{\sigma\bar{\sigma}}\rho_{\sigma}\rho_{\bar{\sigma}} \tag{12}$$

2.4. He-Chen-Zhang (HCZ)

The HCZ formulation (He et al., 1999), similar to MPSC, simulates two phases of a single component; however, the distribution of the two phases is handled with a more elaborate scheme using two PDFs, one of which tracks the fluid properties, similar to previous approaches, while the other represents the phase field and thus tracks the interface between fluids. To describe the phase-field evolution, three different governing equations can be employed: Cahn–Hilliard, Allen–Cahn, or Sun and Beckermann (Hu et al., 2020). In this study, as in He et al. (1999), the Cahn–Hilliard one is used. The equations presented below are based on those described in Huang et al. (2015), Wang and Peng (2020), and Yuana et al. (2021), although the original formulation originates from He et al. (1999). Eq. (13) accounts for the distribution of particle densities, while Eq. (14) tracks the interface between phases, each based on its own relaxation time. The source terms are calculated respectively by Eqs. (15) and (16).

$$\begin{aligned} &g_i\left(\mathbf{x}+\mathbf{e_i}\Delta t, t, t+\Delta t\right) \\ &= g_i(\mathbf{x},t) - \frac{1}{\tau_1}\left(g_i(\mathbf{x},t) - g_{eq}(\mathbf{x},t)\right) + S_i(\mathbf{x},t) \end{aligned} \tag{13}$$

$$\begin{aligned} &f_i\left(\mathbf{x}+\mathbf{e_i}\Delta t, t+\Delta t\right) = \\ &f_i(\mathbf{x},t) - \frac{1}{\tau_2}\left(f_i(\mathbf{x},t) - f_i^{eq}(\mathbf{x},t)\right) + S_i'(\mathbf{x},t) \end{aligned} \tag{14}$$

$$\begin{aligned} S_i = &\left(1-\frac{1}{2\tau_1}\right)\left(\mathbf{e_i}-\mathbf{u}\right)\left(\kappa\rho\mathrm{d}(\nabla^2\rho)+\mathbf{G}\right)\Gamma_i(\mathbf{u}) \\ &+\left(1-\frac{1}{2\tau_1}\right)\left(\mathbf{e_i}-\mathbf{u}\right)\left(-\mathrm{d}\psi(\rho)\right)\left[\Gamma_i(\mathbf{u})-\Gamma_i(\mathbf{0})\right] \end{aligned} \tag{15}$$

$$S_i' = \left(1-\frac{1}{2\tau_2}\right)\frac{\left(\mathbf{e_i}-\mathbf{u}\right)}{c_s^2\rho}\left(-\mathrm{d}\psi(\phi)\right)f_i^{eq} \tag{16}$$

The auxiliary variables used for the calculations of the source terms are:

$$\Gamma_i(\mathbf{u}) = f_i^{eq}/\phi \tag{17}$$

$$\psi(\rho) = p - c_s^2\rho \tag{18}$$

$$\psi(\phi) = p_{th} - c_s^2\phi \tag{19}$$

Regarding the equilibrium distribution functions used at the collision step, f_{eq} is calculated by Eq. (2) with ρ replaced by ϕ, while g_{eq} is calculated by Eq. (20).

$$g_i^{eq}(\mathbf{x},t) = w_i\left[p + c_s^2\rho\left(\frac{\mathbf{e_i}\cdot\mathbf{u}}{c_s^2} + \frac{(\mathbf{e_i}\cdot\mathbf{u})^2}{2c_s^4} - \frac{\mathbf{u}^2}{2c_s^2}\right)\right] \tag{20}$$

The macroscopic variables for the index function, velocity, and pressure are defined by Eqs. (21), (22), and (23).

$$\phi = \sum f_i \tag{21}$$

$$\rho\mathbf{u}c_s^2 = \sum \mathbf{e_i}g_i + \frac{\Delta t}{2}c_s^2(\kappa\rho\mathrm{d}(\nabla^2\rho) + \mathbf{G}) \tag{22}$$

$$p = \sum \bar{g}_i + \frac{\Delta t}{2}\mathbf{u}(-\mathrm{d}\psi(\rho)) \tag{23}$$

An EoS is again required, this time for calculating p_{th} and not macroscopic pressure, which is already given by Eq. (23). In this study, Carnahan–Starling is used in accordance to He et al. (1999). Eq. (24) presents this EoS in the context of this method. The liquid–gas coexisting values of ϕ, ϕ_l and ϕ_g, are determined by the Maxwell construction and the chosen EoS. Based on these values, the density can be obtained from Eq. (25). In this study, the liquid and gas coexistence densities are chosen as $\rho_l = \phi_l$ and $\rho_g = \phi_g$, respectively, to simplify the mapping, making $\rho = \phi$.

$$p_{th} = \phi c_s^2\frac{1 + b\phi/4 + (b\phi/4)^2 - (b\phi/4)^3}{(1-b\phi/4)^3} - a\phi^2 \tag{24}$$

$$\rho(\phi) = \rho_g + \frac{\phi-\phi_g}{\phi_l-\phi_g}\left(\rho_l - \rho_g\right) \tag{25}$$

3. Calibration of interfacial properties

To correctly compare the performance of the three selected methods in capturing fluid distributions in unsaturated soil, the first step is to ensure that the same relevant physical properties are represented across all methods. This study focuses on conditions representative of fine-grained granular soils, for which capillary forces dominate over gravitational forces, allowing gravity to be neglected, and on quasi-static processes, for which viscous and inertial effects are negligible. Under these conditions, fluid behavior is governed primarily by capillarity, and the dominant properties of interest are interfacial properties. According to the Young–Laplace equation, Eq. (26), the capillary suction, ΔP, is controlled by the surface tension, γ, and the principal radii of curvature of the meniscus, r_1 and r_2, which are in turn influenced by the contact angle between the fluids and the solid surface. Consequently, it is essential to ensure that surface tension and contact angle are captured consistently across all methods, so that the comparison that stems from them is fair and meaningful.

$$\Delta P = \gamma\left(\frac{1}{r_1} + \frac{1}{r_2}\right) \tag{26}$$

In LBM simulations, physical quantities are typically expressed in lattice units (l.u.) with Δx and Δt taken as unity. Given that each method has a limited range of parameter values over which numerical stability is maintained, it is impractical to match the absolute value of surface tension in lattice units across all methods. To ensure that simulations performed using the three methods nevertheless correspond to the same physical processes, two approaches can be considered. In the first approach, lattice units are converted to physical units by selecting appropriate conversion factors such that the surface tensions match in physical space. This approach requires different time and mass conversion factors for each method, while the length conversion factor must remain fixed to preserve the same geometric representation. The second approach is based on the recognition that, when comparing fluid distributions in unsaturated soil simulations, matching the absolute value of surface tension is not strictly necessary. In such simulations where the primary mechanism is capillarity, the menisci should satisfy the Young–Laplace equation, for which surface tension controls the magnitude of suction but does not affect the curvature of the interface. The curvature, in turn, is controlled by the contact angle for a given geometry (grain packing), hydraulic history, and saturation. Consequently, if suction is normalized by the surface tension associated with each method, according to Eq. (26), the resulting quantity is a

Table 2
Comparative summary of the three multifluid LBM formulations employed in this study.

Method	Multifluid type	Multifluid treatment	Conceptual assumption	Number of PDFs	Complexity of equations	Typical advantage	Computational cost
MPSC	Multiphase	Inter-particle force	Phase separation of a single component governed by a non-ideal EOS	1	Moderate	Simple implementation	Lower
MCSC	Multi-component	Cohesion and adhesion forces	Interaction between independent fluid components	2	Moderate	Independent fluid properties can be specified	Higher
HCZ	Multiphase	Phase-field tracking	Separate tracking of density and interface	2	High: involves $\nabla(\nabla^2)$	Improved thermodynamic consistency	Higher

Table 3
Simulation parameters.

Method	Relaxation parameter	Multifluid parameters				Solid parameters	
MPSC	τ	EoS				ρ_{solids}	
	1	Inputs		Resulting coexistence densities		0.25	
		$a = 1,\ b = 4,\ R = 1,\ T/T_c = 0.7$		$\rho_g = 0.02$	$\rho_l = 0.34$		
MCSC	$\tau_\sigma = \tau_{\bar{\sigma}}$	$G_{\sigma,\bar{\sigma}}$		Input component densities		$G_{ads,\sigma} = -G_{ads,\bar{\sigma}}$	ρ_{solids}
	1	1.00		$\rho_\sigma = 0.03$	$\rho_{\bar{\sigma}} = 2.00$	0.68	1.00
HCZ	$\tau_1 = \tau_2$	k	EoS			$\phi_{solids} = \rho_{solids}$	
	1	10^{-4}	Inputs	Resulting coexistence indices/densities		0.210	
			$a = 12RT = 4,\ b = 4$	$\phi_g = \rho_g = 0.024$	$\phi_l = \rho_l = 0.251$		

representative mean curvature of the system that is directly comparable across different methods, provided that the contact angle is consistent. This approach provides a more general way of comparing results among different methods, or between simulated and experimental results, that does not rely on particular choices for unit conversion. The latter approach is adopted in the present study.

The procedures used to measure surface tension and contact angle are described below. The overall calibration procedure is summarized in Fig. 1, with the details of each step explained in the following subsections. The input parameters used for each method are summarized in Table 3. The relaxation and multifluid parameters were selected based on values commonly reported in the literature. For all multifluid LBM methods considered, viscosity is determined by the relaxation time, which was chosen based on literature recommendations to ensure numerical stability. Because the analyses presented here focus on quasi-static processes, the viscosity ratio between the two fluids does not influence the equilibrium interface configuration and was therefore set to unity in this study. Based on the selected multifluid properties, the calibrated values of surface tension are first established for each method, after which the solid parameters are adjusted to ensure that all methods reproduce the same contact angle, resulting in the values reported in Table 3. All quantities in the following subsections are expressed in lattice units (l.u.).

3.1. Surface tension

In most multifluid LBM approaches, surface tension is not a direct input parameter; rather, it emerges indirectly from other modeling parameters, particularly those listed in the multifluid parameters column of Table 3. Consequently, the common approach for determining surface tension for a given set of model parameters is to simulate a simple configuration for which the Young–Laplace equation can be readily applied, and to back-calculate the surface tension from the measured suction and interface curvature. This procedure is commonly referred to as the Young–Laplace test.

The most widely used Young–Laplace test in the literature is the simulation of a single 2D or 3D bubble (Pan et al., 2004; Zhang et al., 2000; Zhao et al., 2021; Zhu et al., 2024; Nekoeian et al., 2018). As an illustrative example, consider the schematic 2D bubble shown in Fig. 2a, along with the corresponding density profile shown in Fig. 2b. In such simulations, the pressures associated with the bulk liquid and gas phases, corresponding to the densities ρ_l and ρ_g measured sufficiently far from the interface, can be used to compute the pressure difference ΔP. In addition, the bubble radius, R, can be determined geometrically and used to evaluate the mean curvature, $1/r_1 + 1/r_2$. For a 2D bubble, $r_1 = R$ and $r_2 = \infty$, such that the mean curvature reduces to $1/R$. By repeating this procedure for bubbles of different radii, a set of suction–curvature data points can be obtained, as illustrated in Fig. 2c. According to the Young–Laplace equation, fitting a linear relationship to these data yields a slope equal to the surface tension.

While this is a convenient method for measuring surface tension, the bubble configuration differs from the fluid distributions encountered between soil grains, where the liquid phase is typically attracted to the solid surface and the liquid pressure is lower than the gas pressure. To better reflect these conditions, Hosseini et al. (2024) used an alternative Young–Laplace test based on a liquid bridge formed between two parallel solid plates, a schematic of which is shown in Fig. 3. In this configuration, the liquid bridge is more representative of the fluid distributions of interest in unsaturated soils. Similar to the bubble test, the pressures in the two phases and the meniscus curvature can be measured, and the resulting data can be plotted analogously to Fig. 2c to determine the surface tension.

For completeness, both tests were employed in this study and compared, which shed light on an important aspect: the choices of threshold density. As illustrated in Fig. 2b, the density profile across the interface is smooth, and the interface is diffuse rather than sharp, a behavior that applies to all methods considered in this study. However, to define the radius of the bubble or the meniscus, a specific interface location must be selected. In LBM studies, it is common practice to select some threshold density, $\rho_{threshold}$, within the interfacial region and to use this value consistently across simulations. The implicit assumption is that, if the $\rho_{threshold}$ used in the simulations matches that employed in the Young–Laplace test, the surface tension obtained from the Young–Laplace test will also be applicable to the simulations. However, the results of this study indicate that the surface tension values inferred from the bubble test do not match those obtained from the plate

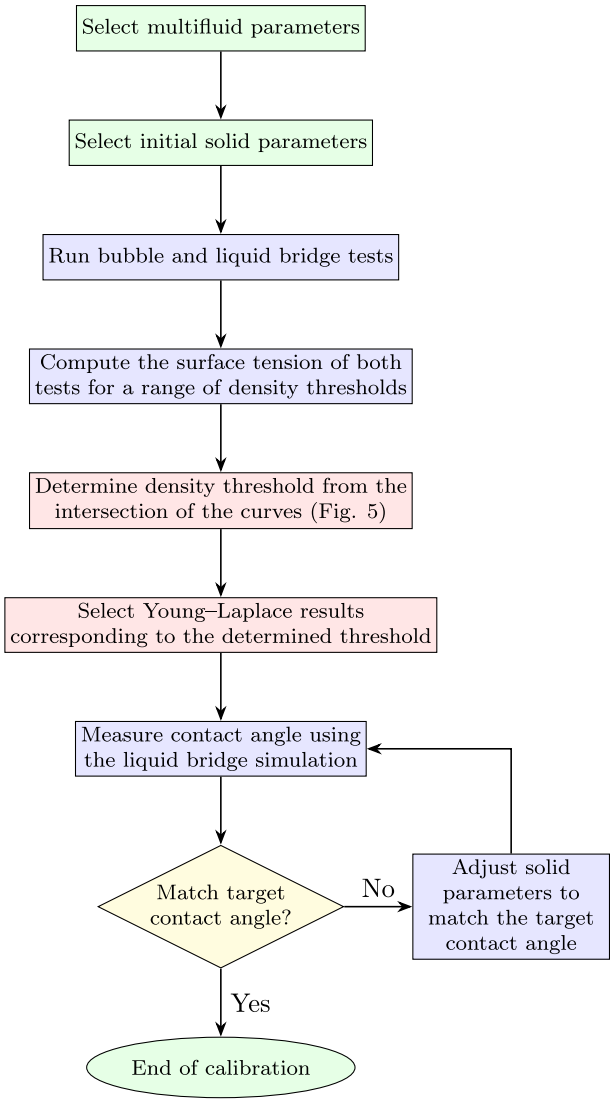

Fig. 1. Flowchart of the suggested calibration method focusing on threshold density determination.

test for all choices of $\rho_{threshold}$. Therefore, before presenting the final Young–Laplace test results, the procedure used to select $\rho_{threshold}$ is discussed.

3.1.1. Threshold density

Different approaches for selecting threshold values are reported in the literature, often involving simply adopting a proportion of the bulk densities. Some studies, such as Huang et al. (2011) for MPSC and Huang et al. (2007), Sukop and Thorne (2005) and Zhao et al. (2021) for MCSC, define the threshold as the average value between ρ_l and ρ_g. Alternatively, Zhou et al. (2020) proposed a threshold density of half the density of the fluid forming the structure of interest, typically a droplet.

In this study, a more systematic approach is adopted. As illustrated in Fig. 4, decreasing $\rho_{threshold}$ shifts the identified interface toward the gas phase, resulting in an increase in the measured bubble radius (Fig. 4a), while producing the opposite effect on the meniscus radius in the liquid bridge (Fig. 4b). This behavior suggests that there exists a value of $\rho_{threshold}$ for which the surface tension values inferred from the two tests coincide. Accordingly, both tests were performed over a range of $\rho_{threshold}$ values, and the resulting surface tension estimates

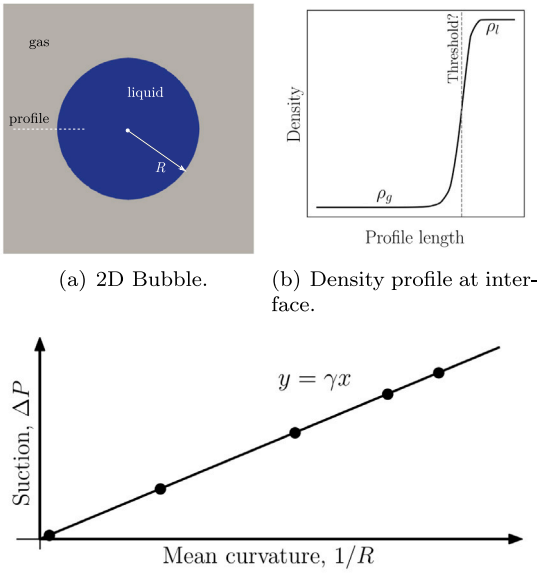

(a) 2D Bubble. (b) Density profile at interface.

(c) Schematic Young-Laplace test results.

Fig. 2. Young–Laplace test using a 2D bubble.

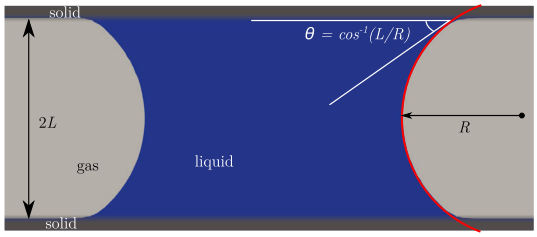

Fig. 3. Young–Laplace test using a 2D liquid bridge between two plates separated by a distance 2L. R denotes the meniscus radius of curvature and θ is the contact angle between the liquid and the solid.

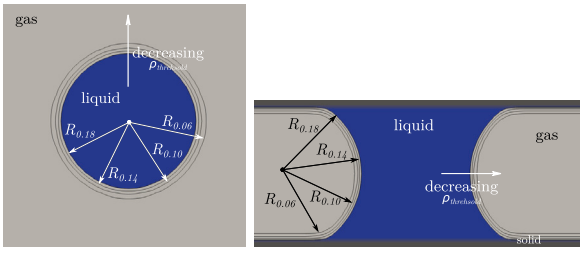

(a) Bubble. (b) Liquid bridge between plates.

Fig. 4. Influence of the threshold density, $\rho_{threshold}$, on the radius of curvature. The subscripts of the radii, R, represent the $\rho_{threshold}$ used in the MPSC method, corresponding to the values in Fig. 5.

were plotted together to identify their intersection. Example results are shown in Fig. 5 for the MPSC method, indicating that a $\rho_{threshold}$ of 0.12 yields consistent results between the two tests. The same procedure was applied to the other methods, resulting in thresholds of 0.7 for MCSC and 0.175 for HCZ. Fig. 1 presents a flowchart of the proposed method.

The broader implication of these results, beyond the calibration performed in the present study, is that the common assumption that surface tension values obtained from a bubble test directly apply to simulations involving solid boundaries is not strictly valid for arbitrary choices of $\rho_{threshold}$. For example, considering the MPSC results shown

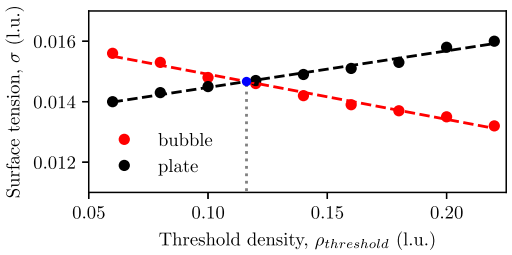

Fig. 5. Measured surface tension from the Young–Laplace tests using both bubble and plate configurations versus threshold density, for MPSC.

in Fig. 5, if surface tension were determined solely from the bubble test and $\rho_{threshold}$ were selected using the conventional choice of the average between the liquid and gas densities, equal to 0.18 in this case, the resulting surface tension would be approximately 13% lower than the value effectively experienced by the model in simulations involving solid surfaces. While such discrepancies may be acceptable for purely qualitative studies, they become important for quantitative investigations, particularly those involving comparisons with experimental data or comparisons across different numerical methods, as is the case in the present study. It is worth noting that, moving forward, it is not strictly necessary to employ the two-test calibration procedure adopted here unless the problem of interest involves the coexistence of both bubbles and menisci, requiring a consistent surface tension across different liquid structures. For unsaturated soil problems, where the liquid phase is predominantly present in the form of menisci, using only the plate test, which more closely resembles the actual physical configuration, should be sufficient; in this case, the specific choice of $\rho_{threshold}$ becomes less critical, provided it is applied consistently across all simulations.

3.1.2. Young–Laplace test results

The results of the Young–Laplace tests for both the bubble and plate configurations using a consistent choice of $\rho_{threshold}$, are presented in Fig. 6 for all three methods. All trendlines are forced to pass through the origin to remain consistent with Eq. (26). The slopes of the lines indicate the measured surface tension in lattice units. Note that the measured surface tension values apply specifically to the input parameters listed in Table 3.

An important observation is that different methods respond differently to resolution (bubble or meniscus size). For MPSC, the data points follow the expected linear trend even at high values of $1/R$ (corresponding to small bubbles or menisci). For MCSC, the data points exhibit some scatter at high $1/R$, but a linear trendline can still be fitted. In contrast, for HCZ, data points with $1/R$ greater than approximately 0.25 deviate significantly from the linear trend; consequently, these points were excluded from the fitting. This behavior highlights the sensitivity of the HCZ method to resolution, as high $1/R$ corresponds to smaller bubble radii or smaller plate spacings, which are analogous to lower spatial resolution in simulations. This observation is consistent with the behavior of HCZ simulations discussed in the following sections.

Another important observation is that the bubble test can only be performed reliably in the low-curvature (large-bubble) limit. Attempts to simulate smaller bubbles showed that, as curvature increases, the diffuse interface becomes too thick relative to the bulk fluid region, preventing accurate determination of bulk densities and pressures. This limitation is consistent with bubble tests reported in the literature, where the curvature axis typically does not extend beyond values of approximately 0.1. In contrast, simulations of unsaturated soils or multiphase flow in porous media often involve curvatures exceeding 0.5 at low saturations, unless extremely high spatial resolutions (i.e., a very large number of grid points) are employed, which is computationally

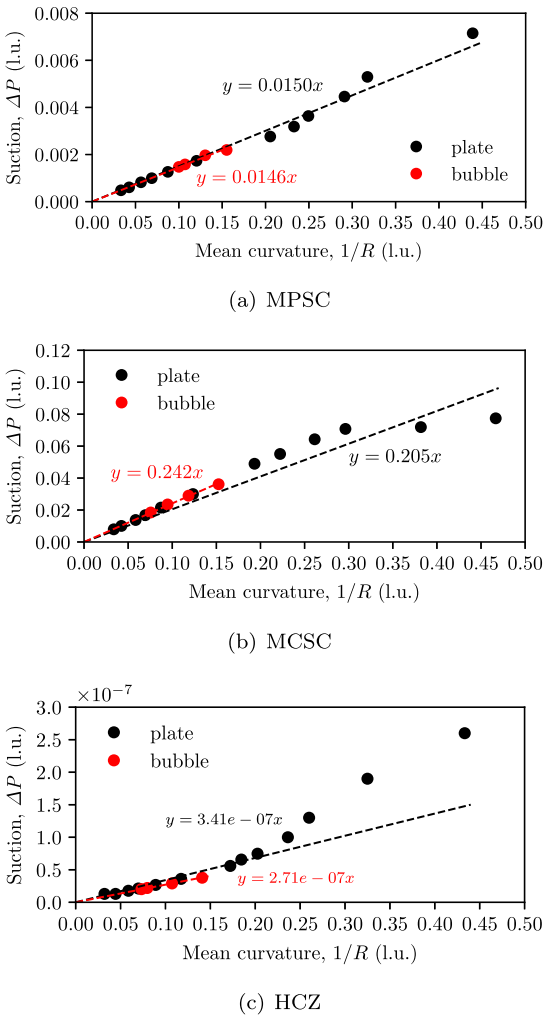

Fig. 6. Young–Laplace test results for both bubble and plate configurations.

impractical in most cases. The plate test does not suffer from this limitation because, even at high curvature corresponding to small plate spacing, the liquid bridge is not laterally confined (unlike a bubble that must contract in all directions), allowing a well-defined bulk region to form within the bridge.

3.2. Contact angle

The contact angle between the fluids and the solid surface is controlled by different input parameters depending on the multifluid method. To establish the relationship between the relevant input parameters and the resulting contact angle, a parametric study was performed by systematically varying these parameters and measuring the contact angle using the same plate test described in the previous subsection. The contact angle, θ, was determined from the relationship between the plate spacing and the meniscus radius, as illustrated in Fig. 3. The results of this analysis are shown in Fig. 7. In practice, this calibration only needs to be performed for the selected multifluid parameters used in the simulations, with only the solid parameters varied. The parametric study is nevertheless presented here over a wider range of multifluid parameters for completeness.

In MPSC, the parameter used to control the contact angle is the density assigned to the solids, ρ_{solids}. This density determines the magnitude of the interaction force between the fluid and the solid nodes. The imposed density should be set between the density of the gas and

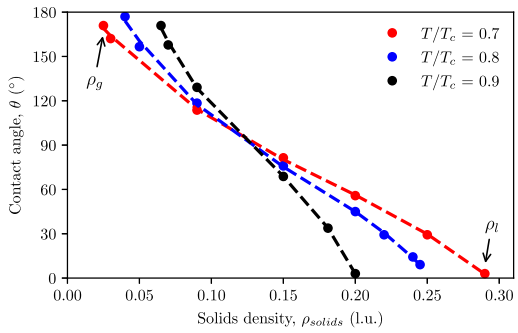

(a) MPSC

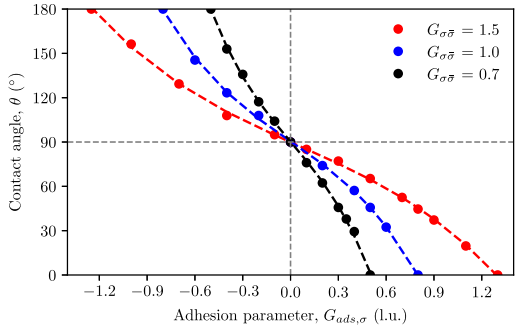

(b) MCSC

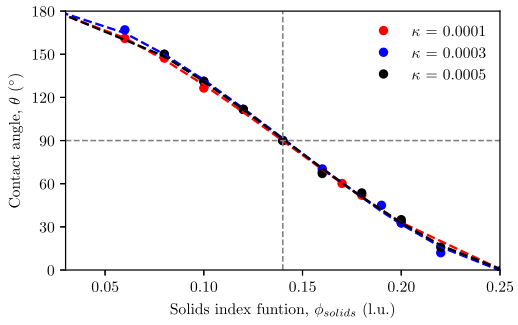

(c) HCZ

Fig. 7. Parametric study of contact angle.

the liquid phases (Shan and Chen, 1993; Martys and Chen, 1996; Shan and Doolen, 1995). Fig. 7a presents this analysis. It can be observed that assigning $\rho_{solids} = \rho_l$ results in a contact angle of 0°, corresponding to complete wetting, whereas assigning $\rho_{solids} = \rho_g$ yields a contact angle of 180°, corresponding to a fully hydrophobic surface. Therefore, the entire range between 0 and 180° can be achieved by adjusting this input parameter.

In MCSC, both $G_{\text{ads},\sigma}$ and ρ_{solids} affect the contact angle; however, $G_{\text{ads},\sigma}$ provides better control over the full range of contact angles. Therefore, it is preferable to keep ρ_{solids} constant and only use $G_{\text{ads},\sigma}$ to tune the contact angle. For a constant ρ_{solids} of 1.0, the results of the parametric study are shown in Fig. 7b. Similar to MPSC, the entire wettability range can be achieved by varying $G_{\text{ads},\sigma}$, with a value of 0 corresponding to neutral wetting ($\theta = 90°$). For this method, Huang et al. (2007) also performed contact-angle studies and proposed Eq. (27) to estimate the contact angle prior to simulation. The densities ρ_σ and $\rho_{\bar{\sigma}}$ correspond to the input densities of the fluid components. When similar cohesion and adhesion parameters and comparable initial densities were employed, the results of the present study were consistent with those of Huang et al. (2007) and with the predictions of their equation. To achieve such agreement, however, ρ_{solids} must be set to 0.2, as this parameter also influences the contact angle in the MCSC model but is not accounted for in Eq. (27). An example of the effect of ρ_{solids} in the achieved contact angle is provided in Appendix. Comparable results regards the influence of $G_{\text{ads},\sigma}$ on the contact angle are presented by Jansen et al. (2013).

$$\cos\theta_{\sigma\bar{\sigma}} = \frac{G_{\text{ads},\sigma} - G_{\text{ads},\bar{\sigma}}}{G_{\sigma\bar{\sigma}}\frac{\rho_\sigma - \rho_{\bar{\sigma}}}{2}} \tag{27}$$

In HCZ, the controlling parameter for contact angle is ϕ_{solids}, which is the value of the index function imposed to the solid nodes. Fig. 7c presents the variations of θ as a function of ϕ_{solids} for different κ values. Similar to MPSC, the contact angle is 0° for $\phi_{solids} = \phi_l$ and 180° for $\phi_{solids} = \phi_l$. Yiotis et al. (2007) also performed contact angle sensitivity analyses for this method and obtained similar trends. In their study, they relate contact angle to the imposed solids density with a linear fit, however, we find that a third degree polynomial is a better fit to the results in Fig. 7c, and upon closer examination, it also represents the data reported by Yiotis et al. (2007) more accurately.

For the simulations in this study, a contact angle of 30° was selected based on typical values reported for quartz surfaces (Chen et al., 2015). Accordingly, the parameters in the solid-parameters column of Table 3 were chosen to correspond to this contact angle for the selected multifluid parameters, based on the results shown in Fig. 7.

3.3. Verification: two solid grains

Given that the general problem of interest involves a granular packing representing soil, it is important to validate the methodology described above when applied to a multigrain configuration with more complex surface geometries. For a liquid bridge between two grains, which the simplest multigrain unsaturated scenario, both the radius of curvature and the suction can be measured, enabling an analytical calculation of the surface tension to compare with the numerical results.

A 2D simulation of a meniscus between two grains of diameter 12 was performed, with their centers spaced 25 apart, as illustrated in Fig. 8 for MPSC. The radius of curvature obtained was R of 9, which was substituted in Eq. (26), together with the surface tension previously determined of 0.015. The suction value obtained was 0.001684, which is compatible with the simulation output of 0.001701. The same consistency was observed for the other two methods. These results indicate that the threshold and surface tension values obtained from the calibration tests also produce consistent curvature and suction estimates in a two-grain configuration, suggesting that they can be applied to geometries composed of multiple curved grain surfaces, provided that sufficient spatial resolution is maintained.

4. Simulation setup

4.1. Geometry and boundary conditions

To compare the different methods in terms of their ability to simulate fluid distributions in unsaturated soils, a 2D granular packing is employed. This configuration is chosen over a 3D one because it enables clearer visualization and comparison of phase distributions, while also being computationally more efficient. This efficiency allows a more systematic and detailed exploration of the results through multiple simulation runs. To reproduce pore emptying and filling processes in two dimensions, the grains must be sufficiently spaced to allow fluid movement between them. Following this requirement, the 2D packing shown in Fig. 9 was constructed to include a range of pore sizes and throat widths (i.e., narrow constrictions between adjacent grains). The grains are assumed to be perfectly round and fixed in space. A grid size of 200 × 200 is assigned to the packing. This grid size is chosen such that the major throats, which are expected to allow pore emptying,

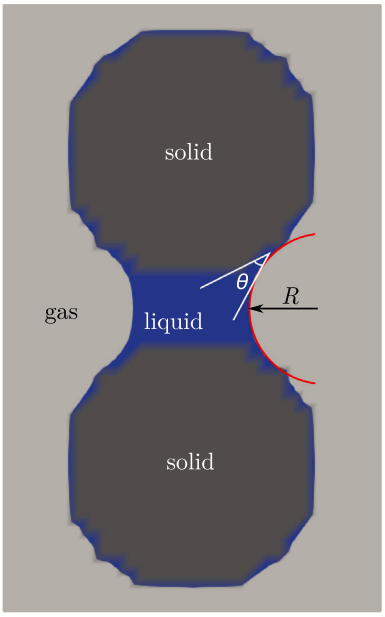

Fig. 8. MPSC 2D simulation of a liquid bridge between two grains.

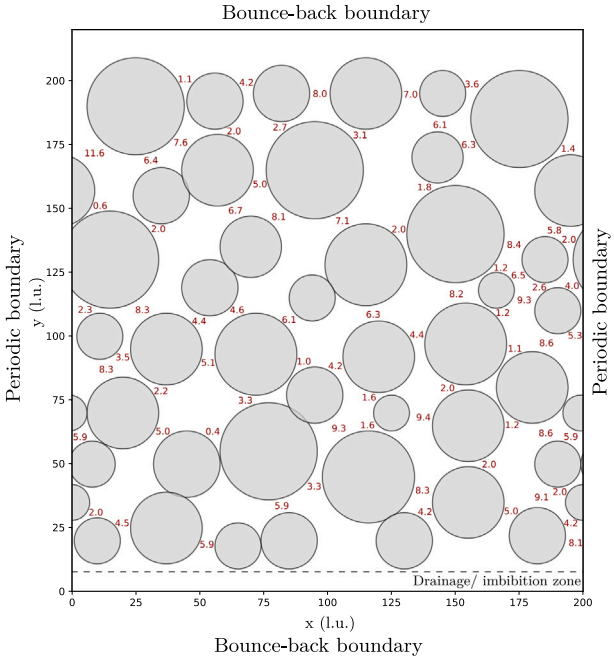

Fig. 9. 2D grain packing: positioning, boundary conditions and throat diameters. Porous plate is indicated by the dashed line.

have a resolution of at least four lattice spacings. The throat sizes based on this grid size are labeled in Fig. 9.

The figure also shows the boundary conditions employed. Periodic boundary conditions were applied on the lateral sides to ensure system continuity where no fluid imbibition or drainage occurs. Bounce-back conditions were used at the top and bottom to prevent fluid communication across those boundaries. The top boundary has been placed far away from the surface of the grains to allow an air layer to form on the top. A porous plate is placed beneath the grain assembly, with three lattice spacings in its openings, corresponding to an air-entry curvature (proxy for air-entry value, AEV) of 0.58, given a contact angle of 30°.

4.2. Initialization, drainage, and imbibition

To initialize the simulation, the samples were first fully saturated by the wetting phase, i.e., liquid, with a thin layer of the non-wetting phase, i.e., gas, placed above it. From this initial state, the samples were drained until the air penetrated the porous plate, and subsequently re-imbibed until full saturation was restored.

To induce drainage and imbibition, negative or positive density increments were applied, respectively, to the nodes below the porous plate at fixed intervals. Because pressure in LBM is a function of density, this local density modification introduces a temporary pressure imbalance near the boundary, which drives fluid flow within the domain. As the system evolves, the pressure field redistributes and eventually reaches equilibrium. Although this procedure introduces a pressure imbalance, the test is effectively volume-controlled rather than suction-controlled. Because both the increment and the number of nodes to which the increment is applied are known, the total mass removed from or added to the system can be computed. The test is therefore mass/volume-controlled, since a prescribed change in fluid mass/volume is imposed, and the suction is free to change until equilibrium is reached under these new conditions. This differs from suction-controlled tests, in which suction is imposed and the fluid volume adjusts accordingly until equilibrium is established under the imposed suction. Although other boundary-condition-based approaches exist for inducing drainage or imbibition through imposed suction, such as the non-equilibrium bounce-back scheme (NEBB) (Zou and He, 1997; Zhou et al., 2020; Zhang et al., 2024), they were not adopted in this study for the sake of simplicity.

To ensure that all three methods simulate comparable physical processes, drainage and imbibition were performed slowly, so the system evolves in a quasi-static manner. This guarantees that fluid pressures can equilibrate across the domain before each subsequent drainage or imbibition increment, eliminating any time-dependent effects. Preliminary tests were carried out to determine how quickly each model redistributes pressure, thereby identifying the maximum allowable drainage or imbibition rate that still preserves quasi-static conditions while maintaining computational efficiency. The results indicated that, for MPSC, draining or imbibing with a density decrement/increment of 0.01 applied every 25 000 steps provides sufficient time for equilibration, while for MCSC, a slower rate of 0.0005 every 50 000 steps is required, and for HCZ, 0.002 every 25 000 steps is suitable.

4.3. Suction and saturation calculation

The suction, ΔP, and the degree of saturation, S_w, required for constructing the soil–water retention curve (SWRC), were measured at the end of each drainage/imbibition stage where the sample had reached equilibrium. To calculate suction, the pressure was averaged over nodes located in the bulk region of each fluid. The bulk pressures were obtained by averaging only over nodes whose pressure values lie within a tolerance range around the fluid's maximum or minimum density, thereby excluding fluid–fluid or fluid–solid interface nodes that deviate from true bulk behavior. The density tolerance values employed were 0.5 for MCSC and 0.05 for both MPSC and HCZ. Fig. 10a illustrates this procedure, highlighting the nodes used for calculating suction in the MCSC simulation shown in Fig. 17c (reproduced in Fig. 10b). The saturation was calculated by finding the number of nodes with density above $\rho_{threshold}$, as shown in blue in Fig. 10b, and dividing this value by the total number of fluid nodes in the pore space.

5. Complementary physical model

To provide a qualitative comparison with the numerical results, a simple physical model was constructed by 3D printing the grain configuration used in the simulations, as shown in Fig. 11. The region highlighted by the red box corresponds to the packing shown in Fig. 9,

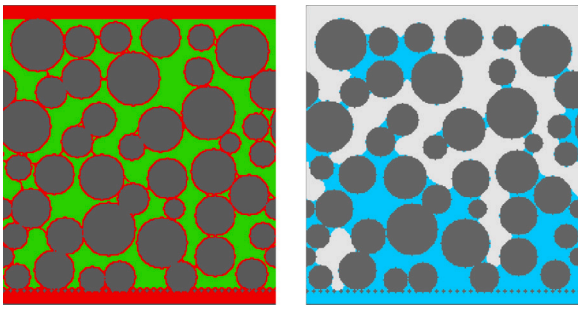

(a) Nodes flagged as bulk (green) or interface (red).

(b) Fig. 17c for reference, showing distribution of liquid (blue) and gas (light gray).

Fig. 10. Node selection for pressure-averaging to calculate suction, shown for the MCSC simulation step presented in Fig. 17c. The bulk nodes are included in the averaging, while the interface nodes are not. Dark gray represents solids.

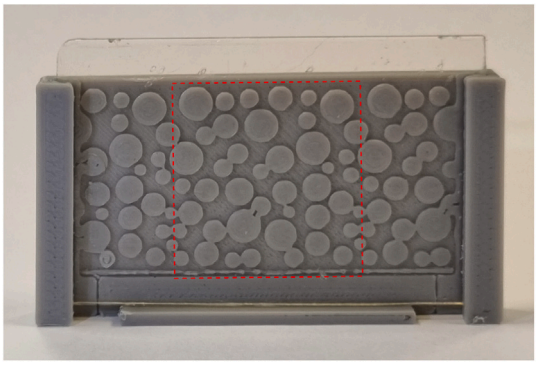

Fig. 11. Physical model including the 3D printed grain configuration (gray) and the sliding transparent plate in the front. The red square corresponds to the domain used in the simulations.

while the surrounding areas were included by assuming periodic extensions of the packing in order to reduce boundary effects. The filament used was PLA (polylactic acid), which has a density of around 1.25 g/cm^3. The contact angle for this material is around 50°, as indicated by the resting droplet on the back of the device in Fig. 12. A scale of 10 lattice units per millimeter was adopted, resulting in a printed domain of approximately 22 × 40 mm. Each disk was printed with a height of 0.2 mm. A transparent sliding plate was placed at the front of the device to allow visualization of the fluid distribution. Two small openings were designed at the bottom boundary to allow drainage, while the top boundary was left open to the atmosphere. Water mixed with blue food dye was used as the working liquid to facilitate visualization of the drainage process. The model was initially fully saturated, consistent with the initial condition used in the simulations. The model was then tilted almost horizontally to reduce the impact of gravity on drainage. During the experiment, gravity alone was observed to not be able to drain the model, and a paper towel was placed in contact with the bottom openings to provide suction, which triggered the beginning of drainage.

Although useful for visualization, this physical model has important limitations. In particular, the simulations assume capillarity-dominated, quasi-static conditions, whereas the physical model is sufficiently large that gravitational forces can play a role. Achieving fully capillarity-dominated behavior in the physical model would require substantially smaller grain sizes; however, further size reduction was not feasible given the resolution limits of the available 3D printer and would also have hindered visualization. In addition, the physical model does not allow precise control of the drainage rate, and transient effects may therefore be present. The lack of such control also prevents quantitative measurements of suction and saturation, and also makes the observation of imbibition impossible. Due to these mechanistic differences, an exact match between the experimental and numerical results is not expected. Nevertheless, the physical model provides a useful qualitative comparison and reproduces several key features of the simulated drainage patterns.

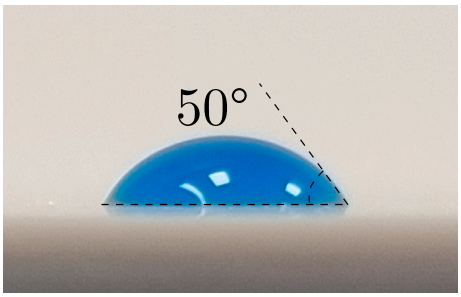

Fig. 12. Measured contact angle between water droplet with blue dye and the 3D printing material (back of the device).

6. Results and discussion

Drainage and imbibition simulations using the three methods, following the setup presented in Section 4, were carried out on the Advanced Research Computing (ARC) TinkerCliffs cluster at Virginia Tech. The TinkerCliffs base compute nodes are equipped with AMD EPYC 7702 processors with 128 cores per node and 256 GB of memory per node. Each simulation used 32 cores on a single node.

This section first presents the SWRC predicted by each method and discusses the physical origin of the oscillations observed in the SWRCs in order to provide context for the subsequent comparisons. Next, the fluid distributions predicted by each method are compared, with primary emphasis on drainage, where the differences between methods are more pronounced, followed by imbibition. The methods are subsequently compared in terms of computational cost. The section concludes with a synthesis of these findings to identify the most suitable method for the capillarity-dominated, quasi-static simulations considered in this study.

6.1. General SWRC and pore-invasion behavior

The resulting drainage SWRCs for each method are shown in Fig. 13, and the corresponding imbibition curves are presented in Fig. 14. Trendlines based on the van Genuchten model (Van Genuchten, 1980) are included in these figures to aid in the visualization of the general trends. Drainage simulations terminated just before air penetrated the porous plate and imbibition simulations were then initiated from this point. For MCSC, this transition occurred at approximately 30% saturation, the reason for which is discussed in Section 6.2.2, whereas MPSC and HCZ were able to drain further, reaching saturations just below 10%. Suction values were normalized by the corresponding surface tension for each method, following the discussion in Section 3 The dashed vertical lines in Figs. 13 and 14 indicate the AEV of the porous plate beneath the grains.

While the general trend of the SWRCs is as expected, the pronounced oscillations during drainage in Fig. 13 may appear unusual. These oscillations arise naturally from the volume-controlled nature of the simulations: in drainage, saturation is prescribed to decrease, whereas no constraint is imposed on the suction, which is therefore free to vary. As liquid is removed from the system, the liquid–gas interface

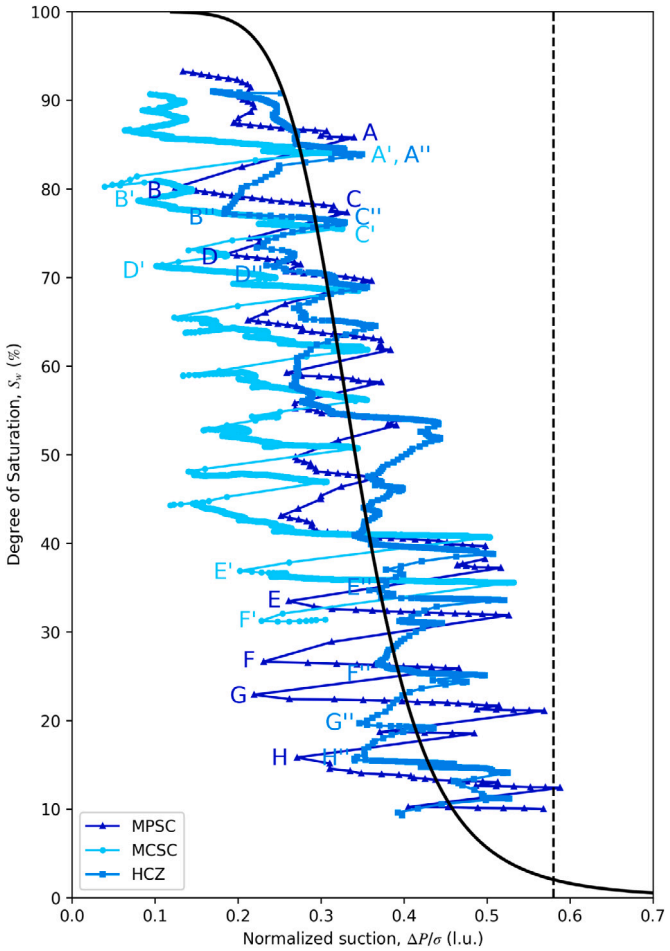

Fig. 13. Simulated drainage SWRCs for the 2D grain packing using the three multifluid methods. The continuous black line is a van Genuchten curve, included to aid in visualizing the general trend. The dashed line correspond to the air-entry value of the porous plate.

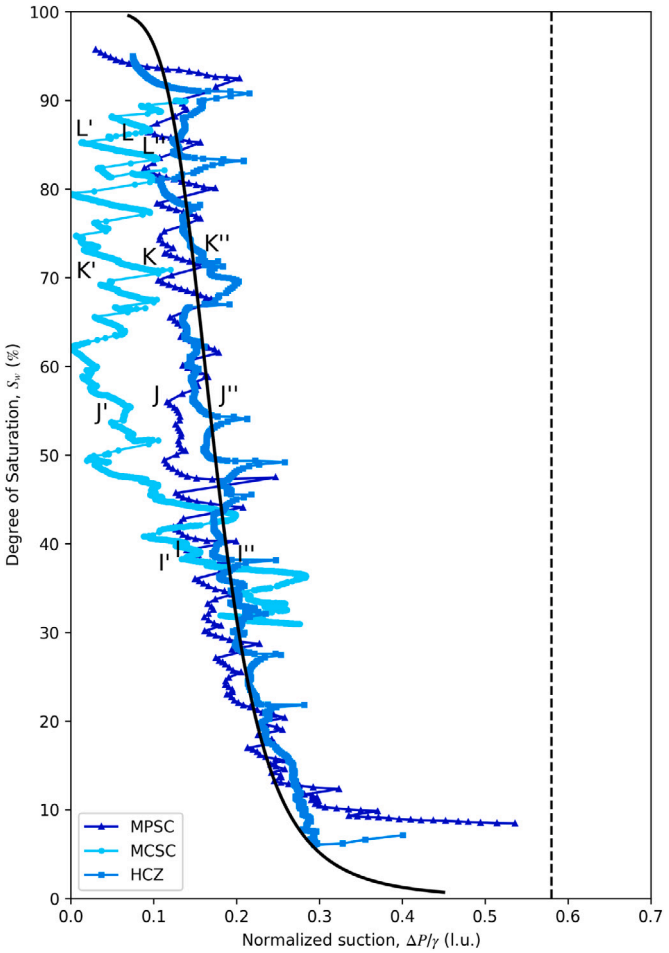

Fig. 14. Simulated imbibition SWRCs for the 2D grain packing using the three multifluid methods. The continuous black line is a van Genuchten curve, included to aid in visualizing the general trend. The dashed line correspond to the air-entry value of the porous plate.

advances into narrow throats, leading to an increase in meniscus curvature and, consequently, suction. Once the interface passes through a throat and enters a larger pore body, the curvature decreases, resulting in a drop in suction. As the interface subsequently approaches the next throat, the meniscus curvature and suction increase again, producing the observed oscillatory behavior. This mechanism is clearly illustrated by the fluid configurations at points A–D in Fig. 15, corresponding to the labeled points in Fig. 13. To facilitate visual comparison across methods, the same shade of blue used to plot SWRC for each method in Fig. 13 is used for the liquid phase in Figs. 15 and 16. A more detailed discussion of this behavior is provided by Hosseini et al. (2024). It should be noted that the oscillations are amplified by the small sample size. In a larger packing containing more grains, multiple invasion pathways are available, and pore invasion is not restricted to a limited number of throats, leading to smoother SWRCs with reduced oscillations, as also shown by Hosseini et al. (2024).

Similarly, the imbibition SWRCs in Fig. 14 exhibit oscillations, but with noticeably smaller amplitude, and are shifted toward lower suction values compared with the drainage curves, forming the expected hysteresis. This behavior arises from the different pore-scale mechanisms governing pore filling and pore emptying. During imbibition, film flow along solid surfaces and capillary condensation at narrow throats promote cooperative pore filling, reducing the need for the interface to pass through narrow constrictions. As a result, the interface curvatures remain more relaxed during imbibition, leading to smoother SWRCs as well as lower suction values at the same saturation, which gives rise to hysteresis between the drainage and imbibition curves. These mechanisms are discussed in greater detail by Hosseini et al. (2024).

Comparing the SWRCs predicted by the three methods, the results span similar suction ranges, exhibit the expected increase in average suction with decreasing saturation, and display comparable hysteresis between drainage and imbibition. Despite these overall similarities, noticeable differences exist between the curves and warrant further examination through the corresponding fluid distributions.

6.2. Comparison of fluid distributions during drainage

The three methods are compared in terms of their ability to capture fluid distributions qualitatively and the associated suction and saturation quantitatively during hydraulic loading. Focusing first on the drainage response, the analysis indicates that the methods exhibit closer agreement at high saturations than at low saturations; accordingly, the following discussion is organized into high- and low-saturation regimes.

6.2.1. High-saturation regime

At high saturations, the three methods exhibit nearly identical pore-invasion behavior. This agreement is evident from the matching oscillations in Fig. 13 and the corresponding fluid configurations shown

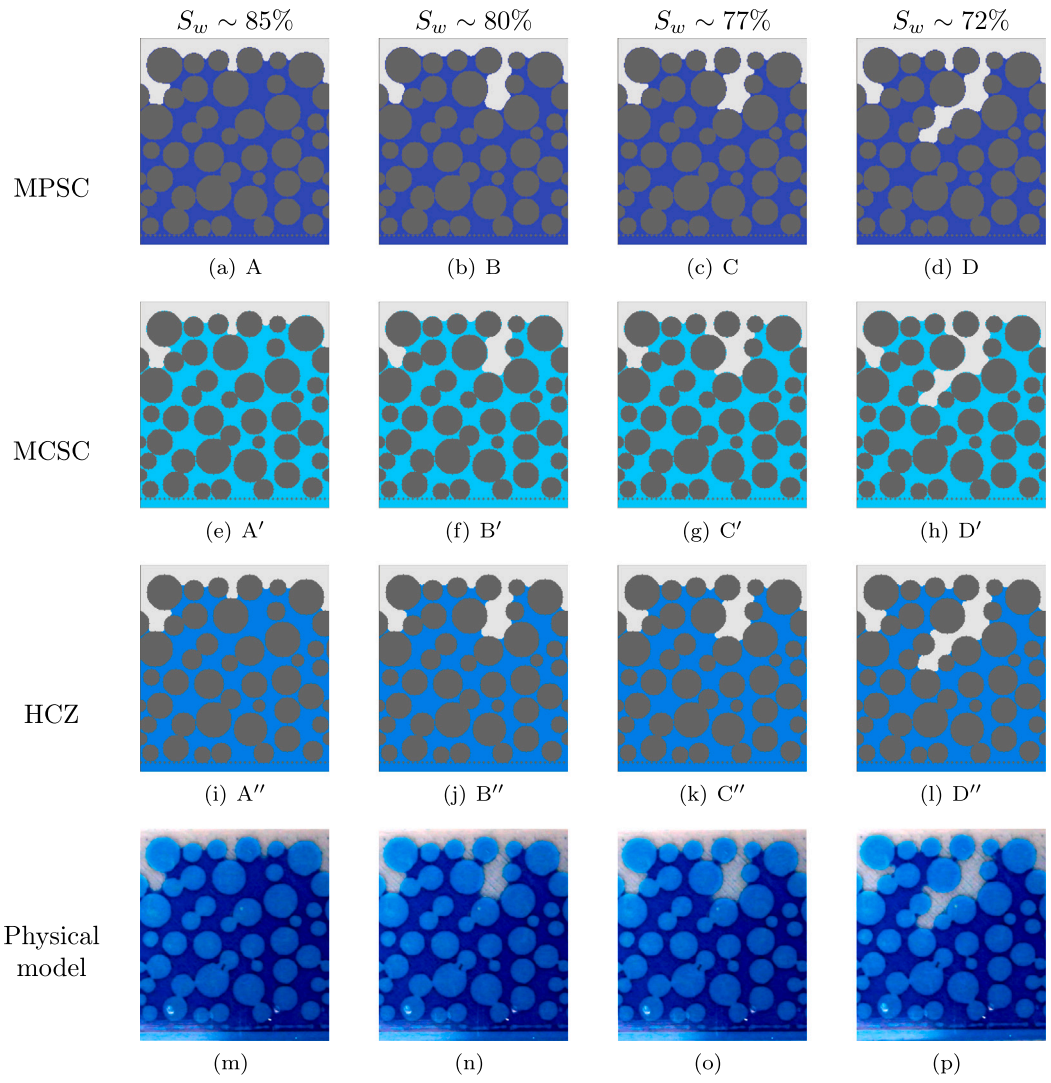

Fig. 15. Fluid distributions at high saturations during drainage for the three multifluid methods and the physical model. The simulation results correspond to the labeled points in Fig. 13.

in Fig. 15. As expected based on capillary considerations, the pore connected to the largest throat is invaded first in region B (second column of Fig. 15) for all methods, followed by invasion of the pore associated with the next-largest throat in region D (last column of Fig. 15). This consistency in the pore-invasion sequence persists down to a saturation of approximately 65%. This invasion pattern also matches that observed in the physical model, shown in the last row of Fig. 15.

While the invasion sequence is consistent across methods, the resulting suction and saturation values do not always coincide. In general, suction values coincide at the peaks of the oscillations, corresponding to moments when the interface advances into a pore throat and the meniscus curvature is maximal, as illustrated in regions A and C (first and third columns of Fig. 15). This indicates that all three methods capture similar air-entry pressures for individual pores. However, once a pore has been invaded and the meniscus curvature relaxes within the pore body, the predicted suction values begin to diverge. Among the three methods, HCZ exhibits the least relaxation and maintains higher suction values, whereas MCSC relaxes the most, resulting in lower suction. These subtle differences in curvature can be observed upon close inspection of the second and last columns of Fig. 15, which correspond to configurations immediately following pore invasion. The resulting variations in curvature and fluid distribution also lead to small differences in saturation between the methods. Nevertheless, despite these minor discrepancies, the overall response predicted by the three methods remains very similar within the high-saturation regime.

6.2.2. *Low-saturation regime*

As saturation decreases, higher suction values and increased meniscus curvatures are required for invasion of the remaining pores. Under these conditions, the numerical resolution, specifically the number of grid points resolving a meniscus, becomes more important, and the responses predicted by the different methods begin to diverge. The two multiphase methods, MPSC and HCZ, exhibit more similar behavior to each other than to the multi-component method, MCSC. Accordingly, the following discussion is divided into two parts: first, a comparison between the two multiphase methods, and second, a comparison between these methods and MCSC.

6.2.2.1. Between the two multiphase methods. Considering the pore-invasion sequences predicted by MPSC and HCZ shown in Fig. 16, both methods begin from similar fluid distributions in the first column and ultimately reach comparable final states in the last column; however, the order of intermediate pore invasions differs between the two. In MPSC, the pore invasion sequence follows the numbered order in Fig. 16d, whereas in HCZ the pores indicated by 3 in the same figure are invaded before 1 and 2. Based on the underlying (pre-discretized) geometry shown in Fig. 9, the throat width associated with pore 1 is

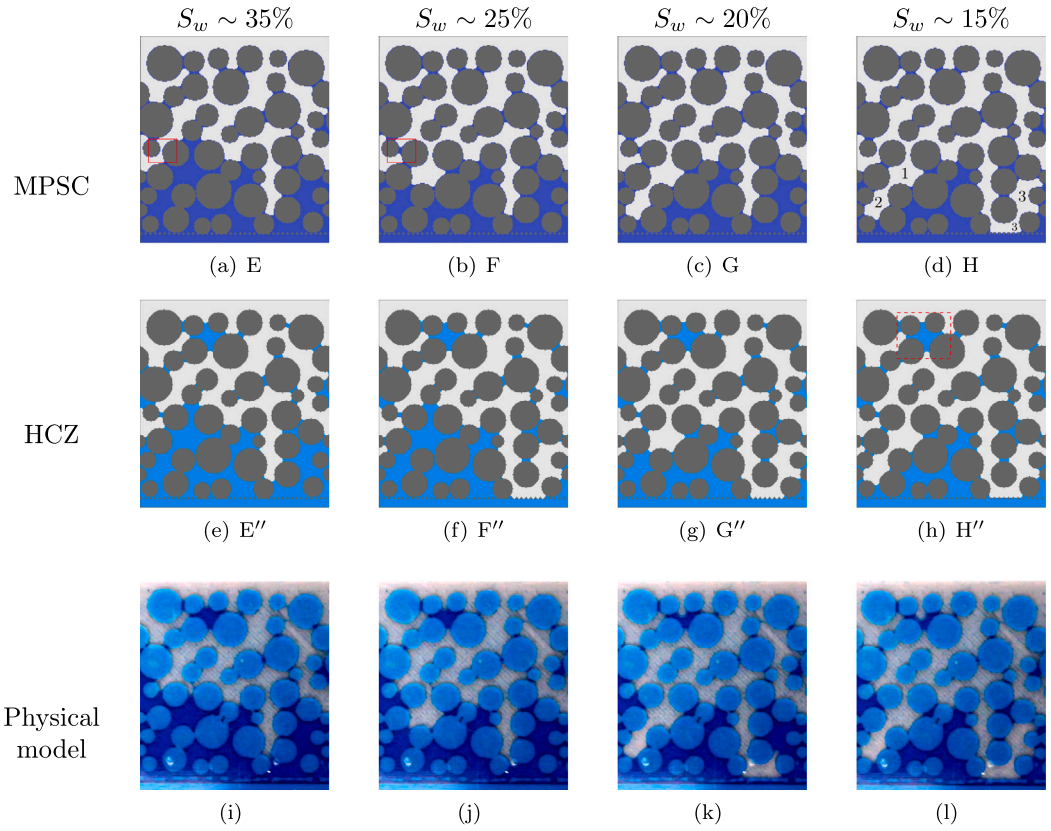

Fig. 16. Fluid distributions at low saturations during drainage for the two multiphase methods and the physical model. The simulation results correspond to the labeled points in Fig. 13.

4.6, which is greater than the throat opening of 4.2 associated with pore 3. Based on Young–Laplace considerations, this would suggest that pore 1 should be invaded before pore 3, as predicted by MPSC. Given that the difference between these throat sizes is smaller than a single grid spacing, the discrepancy in the HCZ prediction can be attributed to numerical resolution effects. This suggests that HCZ is more sensitive to spatial resolution and may require a finer grid to achieve the same level of accuracy in invasion ordering. This observation is consistent with the sensitivity of HCZ observed in the Young–Laplace test presented in Section 3.1.2. These differences in pore invasion order appear at other points along the SWRCs in Fig. 13, contributing to additional oscillations and deviations between the methods. A systematic resolution study could further clarify this behavior by identifying the grid refinement level at which both methods converge to the same invasion order, but is beyond the scope of the present work. The invasion sequence predicted by MPSC is also more consistent with the qualitative trends observed in the physical model, although exact agreement is not expected given the differences between the simulations and the experimental setup discussed previously.

Beyond the invasion sequence, comparison of the upper portion of the domain in Fig. 16, which is drier and corresponds to the pendular regime, indicates that the HCZ method retains a slightly larger volume of liquid, as evidenced by the liquid cluster highlighted by the box in Fig. 16h. This cluster is also observed in the physical model, indicating that HCZ has been more effective in predicting the retained liquid. In contrast, the MPSC formulation occasionally exhibits temporary re-formation of liquid bridges in narrow throats when suction decreases during pore invasion events, as highlighted by the red box in Fig. 16a and b. This behavior is associated with the multiphase pseudopotential formulation, where the two phases remain coupled through the EoS and pressure relaxation following pore invasion can promote local condensation. Aside from these local differences, the two methods predict very similar fluid distributions.

6.2.2.2. Between the multiphase methods and the multi-component method. The fluid distributions at lower saturations predicted by MCSC are shown in Fig. 17. Although the initial fluid configuration in this region is very similar to those predicted by the multiphase methods in the first column of Fig. 16, the subsequent pore-invasion process follows a markedly different path. As in MPSC, pore 1 is the first pore invaded at this stage of drainage. However, unlike the multiphase methods, in which the invaded air remains continuously connected during drainage, the liquid in MCSC refills the throat behind the invaded air, disconnecting it from the continuous air zone and resulting in the formation of an isolated air bubble, as shown in Fig. 17b. With continued drainage, this isolated air bubble becomes the primary feature affected, migrating downward into the next pore (Fig. 17c) until it ultimately penetrates the porous plate (Fig. 17d), at which point the simulation is terminated.

To better understand this behavior, the MCSC simulations were examined in greater detail, with particular focus on (i) the origin of the air-bubble snap-off and (ii) the subsequent downward migration of the air bubble toward the porous plate, despite the presence of pores elsewhere in the domain with lower air-entry values. No definitive physical mechanism could be identified to explain the snap-off event; while snap-off is commonly observed during imbibition, its occurrence during drainage is less typical under quasi-static conditions. Given that this behavior was only observed in the low-saturation, high-suction regime, numerical resolution may be a contributing factor. Regarding the penetration of air into the porous plate, examination of the pressure field during this process (second row in Fig. 16) indicates that the liquid responsible for disconnecting the invaded air exhibits a higher pressure than the liquid zone connected to the bottom boundary. This pressure imbalance may contribute to driving the air bubble downward toward the porous plate. However, the origin of this localized pressure increase remains unclear. Additional simulations performed with progressively reduced drainage rates yielded similar behavior, indicating that the

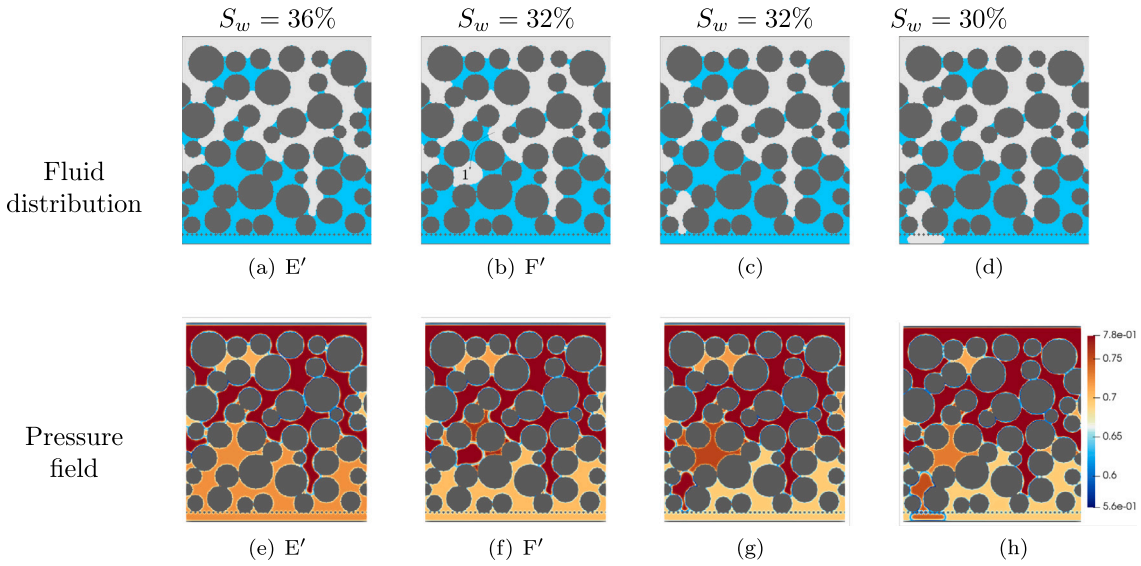

Fig. 17. Simulation results for MCSC at low saturations during drainage, including fluid distributions and pressure fields (in lattice units) corresponding to the labeled points in Fig. 13.

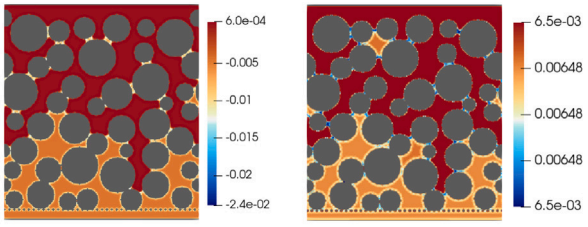

(a) MPSC: E (Subfig. 16a) (b) HCZ: E″ (Subfig. 16e)

Fig. 18. Pressure fields (in lattice units) for MPSC and HCZ at points E and E″ in Fig. 16.

phenomenon is not solely attributable to dynamic forcing. Within the scope of this study, the origin of this behavior could not be determined and requires further investigation.

Another notable difference between the multiphase methods and MCSC emerges in the predicted pressure distributions at low saturations, where liquid bridges and isolated liquid clusters are present. Comparison of the pressure fields predicted by the multiphase methods (Fig. 18) with the pressure field obtained using MCSC at a similar stage of drainage (Fig. 17e) reveals a clear distinction. In the multiphase methods, all bulk liquid regions exhibit the same pressure, even when the liquid phase is disconnected. For example, the pressure within isolated liquid clusters and at the centers of liquid bridges in Fig. 18 matches that of the main liquid body, indicating that the system experiences a uniform suction irrespective of liquid connectivity. In contrast, the MCSC results shown in Fig. 17e indicate that disconnected liquid regions may sustain different pressures. Specifically, isolated liquid clusters in the upper portion of the domain exhibit lower pressures than the main liquid zone, while the centers of liquid bridges exhibit higher pressures. This suggests that, in MCSC, disconnected liquid regions can evolve with independent pressures and, consequently, independent local suctions. This behavior is consistent with the formulation of the multi-component method, in which the two fluid components are modeled independently, unlike in the multiphase approaches where the phases are coupled through a single equation of state across the entire domain. From a physical standpoint, mechanical equilibrium requires the pressure to be uniform within a connected liquid region; however, there is no strict requirement for pressure equality between disconnected liquid bodies. As such, the behavior predicted by MCSC may be physically admissible, although its relevance under quasi-static drainage conditions remains unclear and warrants further investigation. Even if such pressure heterogeneity does occur at the pore scale, its impact on simulations of representative elementary volumes (REVs) may be limited, as microscale pressure variations are expected to be statistically averaged when deriving macroscopic responses. Further studies would be required to assess the significance of this behavior.

6.3. Comparison of fluid distributions during imbibition

The fluid distributions during imbibition are shown in Fig. 19 for the three methods, at varying levels of saturation along the imbibition SWRCs shown previously in Fig. 14. Comparison of the MPSC and HCZ results indicates that the two methods follow slightly different pore-filling pathways during imbibition. In particular, in the HCZ simulations, the gas phase remains continuous throughout the filling process, whereas in MPSC, snap-off events lead to the formation of isolated gas bubbles, as illustrated in Fig. 19c. These bubbles are subsequently filled as imbibition progresses. Despite these differences in the pore-scale filling pathways, the macroscopic responses in terms of the SWRCs shown in Fig. 14 are largely similar. This observation suggests that the mechanisms contributing to hysteresis may differ slightly between the two formulations, even though the resulting SWRCs remain comparable.

In contrast to the multiphase formulations, the MCSC method follows a significantly different imbibition pathway. Because the starting point of MCSC differs from that of the multiphase methods due to the drainage behavior discussed previously, some differences in the initial fluid configurations during imbibition are expected. However, the discrepancies persist even at higher saturations. As shown in the last column of Fig. 19, the fluid distribution predicted by MCSC remains noticeably different from those of the multiphase formulations even at $S_w \sim 85\%$. The pore-filling sequence does not consistently follow the expected capillary order based on pore size, leading to a distinct evolution of the fluid distribution and a somewhat different SWRC compared with the multiphase methods. Examination of the pressure field (not shown) indicates that, similar to the drainage case, significant pressure heterogeneity is present during the early stages of imbibition when multiple liquid clusters exist. As imbibition progresses and the liquid phase becomes more continuous, the pressure field gradually becomes more uniform. Although the macroscopic SWRC

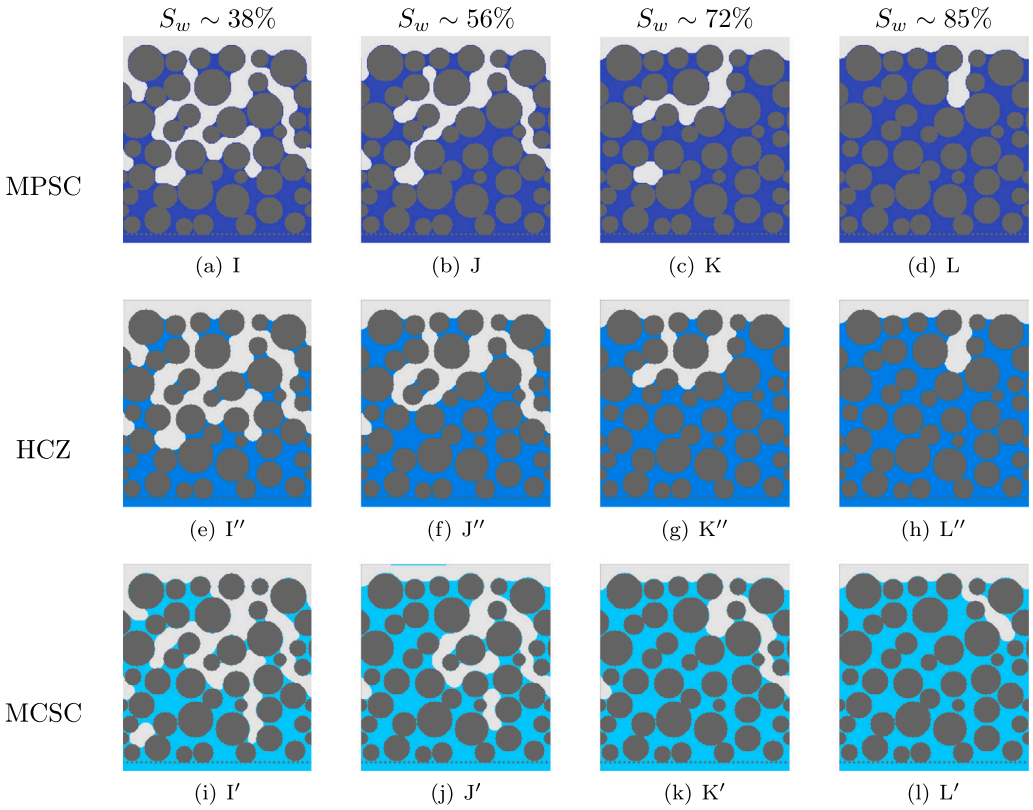

Fig. 19. Fluid distributions during imbibition for the three multifluid methods. The simulation results correspond to the labeled points in Fig. 14.

remains within a comparable range, these pore-scale differences suggest that the MCSC formulation may require further investigation to reliably capture imbibition mechanisms.

6.4. Comparison of the computational cost

The computational cost of each multifluid method for simulating the same problem is governed by two main factors: (i) the computational time required to perform a single lattice timestep and (ii) the number of timesteps required to achieve quasi-static behavior. The former is primarily determined by the algorithmic complexity of each method, whereas the latter depends on the parameterization of the model and on how a single lattice timestep maps to physical time.

With respect to the first factor, the performance of the methods can be compared in terms of MLUPS (million lattice updates per second), a standard metric used to assess the computational efficiency of LBM simulations. For the codes used in this study, which were parallelized on CPUs using OpenMP and executed on comparable hardware, MPSC achieved an average performance of approximately 20 MLUPS, MCSC about 12 MLUPS, and HCZ approximately 0.3 MLUPS. Since all implementations employ similar parallelization strategies, these performance differences can be attributed primarily to intrinsic differences between the methods, such as the number of distribution functions employed and the complexity of the governing equations. While the absolute MLUPS values could be significantly improved through more advanced parallelization strategies, particularly on GPUs, the relative ratios are more relevant here: a single timestep of MPSC is approximately 1.7 times faster than MCSC and about 67 times faster than HCZ.

The second factor concerns the number of timesteps required to reach quasi-static equilibrium. In this study, a range of drainage rates was tested to identify conditions under which the simulated SWRC converged and became insensitive to further reductions in drainage rate. These tests showed that MCSC requires substantially more timesteps than the other methods to achieve equilibrium. For example, considering region C in Fig. 13, where all three methods predict very similar suction–saturation states and comparable fluid configurations (third column in Fig. 15), MPSC required approximately 1.3 million timesteps to reach this state, whereas MCSC required about 276 million timesteps and HCZ approximately 3.5 million timesteps. This indicates that the physical time associated with a single lattice timestep in MCSC is smaller than in the other two methods, necessitating a significantly larger number of iterations to achieve the same quasi-static response.

The combined effect of these two factors leads to large differences in total computational time. For the simulations considered here, MPSC required approximately 2 h to complete the drainage path, making it the fastest method. HCZ required approximately 16 days, while MCSC required roughly 20 days despite covering a smaller saturation range and terminating at about 30%. Although MCSC is closer to MPSC in terms of MLUPS, its substantially larger timestep requirement dominates the overall computational cost, resulting in the longest total runtime. Overall, these results demonstrate a pronounced difference in computational efficiency among the methods, with MPSC being approximately two orders of magnitude more efficient than the other two approaches.

6.5. Assessment of method suitability

Combining the comparisons in terms of fluid-distribution predictions and computational cost allows a clear assessment of the relative merits of the three methods. At high saturations, the differences between the methods are minor. At lower saturations, however, MCSC diverges from the multiphase methods by forming isolated gas clusters and exhibiting heterogeneous pressure distributions, the physical relevance of which under quasi-static drainage conditions remains unclear. Among the two multiphase methods, HCZ appears to be more sensitive to spatial resolution. Although its formulation is, in principle, more thermodynamically consistent, realizing this potential advantage would

likely require substantially higher resolution and, consequently, significantly higher computational cost. Such requirements are impractical when the objective is to simulate unsaturated soil samples of reasonable size. Considering all these factors together, MPSC emerges as the most suitable method for the simulations considered in this study, which focus on capillarity-dominated, quasi-static processes. For other classes of problems, such as those in which gravitational forces are comparable to capillary forces or where transient flow effects are important, density and viscosity ratios can no longer be neglected. In such cases, MPSC offers advantages in representing large density ratios, whereas MCSC allows more straightforward implementation of differing fluid viscosities through component-specific relaxation times. Determining the most appropriate approach for these scenarios requires further investigation; however, it is likely that extending MPSC to account for the necessary density or viscosity contrasts would remain more computationally efficient than adopting MCSC for such applications.

7. Conclusion

Three multifluid extensions of the lattice Boltzmann method were compared, namely the multiphase Shan–Chen (MPSC), multicomponent Shan–Chen (MCSC) and He–Chen–Zhang (HCZ). The application of interest was unsaturated soil, in which air and water coexist in the pore space. After calibrating surface tension and contact angle parameters, drainage and imbibition simulations were performed for a two-dimensional granular packing. The drainage and imbibition rates were chosen to ensure quasi-static conditions, such that time-dependent effects could be neglected. The results obtained with the three methods were compared in terms of pore-scale fluid distributions, as well as global suction and saturation represented by the soil–water retention curve. In addition, a simple physical model was constructed by reproducing the grain configuration using 3D printing, and the pore invasion sequence during drainage was compared with the simulation results.

The results indicate that all three methods capture similar pore invasion sequences at high saturations, with only minor differences in fluid distributions and in the predicted suction and saturation values. At lower saturations, however, the responses diverge. In particular, MCSC predicts a snap-off event that is not observed in the other two methods or in the physical model, and it also exhibits a non-uniform pressure field that is absent in the other approaches. MPSC and HCZ produce broadly similar responses; however, MPSC more accurately predicts the pore invasion sequence expected based on capillary considerations and observations from the physical model. The discrepancy observed in the HCZ results is attributed to sensitivity to numerical resolution. In terms of computational efficiency, MPSC is approximately two orders of magnitude faster than the other two approaches, due to its simpler formulation and the fewer iterations required to reach equilibrium. Considering these factors, MPSC is identified as the most suitable method for the class of problems investigated in this study, which are capillary-dominated and quasi-static. For problems that do not satisfy these conditions, where density and viscosity ratios significantly influence the response, further comparison of the methods is required.

It should be noted that the comparison presented here are based on simulations performed for a single granular packing and a single representative contact angle. However, because the three formulations are applied to the same discretized geometry and physical conditions, moderate variations in contact angle or packing geometry are not expected to significantly affect the qualitative comparison between the methods. In addition, an idealized two-dimensional geometry is used in this study. Further investigation would be required to extend the comparison to fully three-dimensional packings with irregularly shaped particles.

Beyond these extensions, future work aims at comparing the numerical simulation results with experimental results using computed tomography, which would allow assessment of which method captures the most realistic fluid distributions. Another direction of work is coupling the LBM multifluid methods with the discrete element method (DEM), allowing particle motion to be simulated and thereby extending the framework toward more comprehensive soil behavior.

Nomenclature

General LBM

Δt	Time step
$\mathbf{u^{eq}}$	Equilibrium macroscopic velocity
$\mathbf{u}$	Macroscopic velocity
ρ	Macroscopic density
τ	Dimensionless relaxation time
c_s	Lattice sound speed
p	Macroscopic pressure
w_i	Weight coefficients, specific for each DxQy model
$\mathbf{e_i}$	Lattice velocity vector
$f_i(\mathbf{x},t)$	Particle distribution function
$f_i^{eq}(\mathbf{x},t)$	Equilibrium particle distribution function
$S_i(\mathbf{x},t)$	Source term

Multiphase Shan-Chen

$\mathbf{F_{int}}$	Inter-particle force
$\mathbf{F}$	$\mathbf{F_{int}}$ + external forces
$\psi(\mathbf{x},t)$	Mean-field potential
a, b	Carnahan–Starling variables
R	Universal gas constant
T/T_c	Absolute temperature divided by the critical temperature
G	Parameter controlling interparticle force

Multi-component Shan-Chen

$\mathbf{F}_\sigma$	$\mathbf{F_{ads},\sigma} + \mathbf{F_{c},\sigma}$ + external forces
$\mathbf{F_{ads},\sigma}$	Adhesive force between fluids σ and solids
$\mathbf{F_{c},\sigma}$	Cohesive force between fluids σ and $\bar{\sigma}$
$\mathbf{u'}$	Common averaged velocity
$\theta_{\sigma\bar{\sigma}}$	Contact angle between fluids σ and $\bar{\sigma}$
$G_{\sigma\bar{\sigma}}$	Parameter controlling **cohesion** between fluids σ and $\bar{\sigma}$
$G_{ads,\sigma}$	Parameter controlling **adhesion** between fluids σ and solids
$s(\mathbf{x})$	Indicator function for solid (1) or fluid (0)

He–Chen–Zhang

κ	Surface tension controlling parameter
$\mathbf{G}$	External forces
ϕ	Index function
p_{th}	Thermodynamic pressure
f_i	Interface tracking distribution function
g_i	Particle distribution function

CRediT authorship contribution statement

Clara M. Toffoli: Writing – original draft, Visualization, Validation, Software, Investigation. **Reihaneh Hosseini:** Writing – review & editing, Supervision, Project administration, Methodology, Conceptualization. **Jürgen Grabe:** Funding acquisition.

Declaration of competing interest

The authors declare that they have no known competing financial interests or personal relationships that could have appeared to influence the work reported in this paper.

Acknowledgments

The authors acknowledge the funding of this research by the German Research Foundation (Deutsche Forschungsgemeinschaft, DFG) in the framework of project CUS (DFG-2521) at Hamburg University of Technology (TUHH). In addition, we would like to thank our former intern Jayalekshmi Leela for her help with processing simulation results and with the 3D printing.

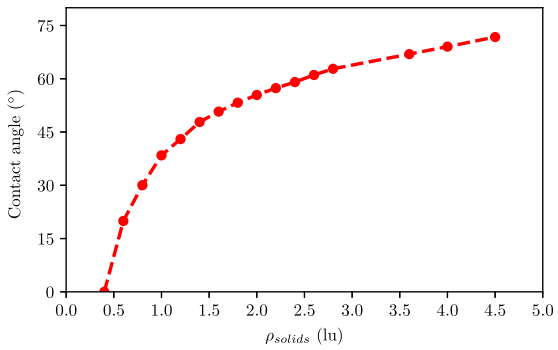

Fig. A.1. Parametric study of contact angle for MCSC by varying ρ_{solids} for $G_{\sigma\bar{\sigma}}$ of 1.3 and a $G_{\text{ads},\sigma}$ of 0.35. The range of ρ_{solids} is bounded by the component densities.

Appendix. Effect of ρ_{solids} on the contact angle in MCSC

The density imposed to the solid wall, ρ_{solids}, is a third parameter that affects the contact angle in MCSC, with $G_{\text{ads},\sigma}$ and $G_{\sigma\bar{\sigma}}$ being the other two. The relationship of this parameter with contact angle is presented in Fig. A.1, for a specific set of $G_{\text{ads},\sigma}$ and $G_{\sigma\bar{\sigma}}$. We would recommend though to keep ρ_{solids} constant at a value between the components densities during simulations and obtain the desired contact angle via $G_{\text{ads},\sigma}$, since not all contact angles are achievable by varying only this variable. Values outside the components densities interval will create a row of air between the liquid bridge and the solid, which is not physical. This indicates that ρ_{solids} can only be set between the components densities, and that unlike in the MPSC presented above, the extremes of this interval will not produce contact angles of 0 and 180°. The relationship between the components densities and the solid density is what determines the contact angle, meaning that a change in the initial density prescribed to them will affect the influence of ρ_{solids} in the contact angle.

Data availability

The code will be made open access, but some general modifications have to be done before that.

References

Benseghier, Z., Millet, O., Philippe, P., Wautier, A., Younes, N., Liberge, E., 2022. Relevance of capillary interfaces simulation with the Shan–Chen multiphase LB model. Granul. Matter 24 (3), 82.

Carnahan, N.F., Starling, K.E., 1969. Equation of state for nonattracting rigid spheres. J. Chem. Phys. 51 (2), 635–636.

Chen, C., Wan, J., Li, W., Song, Y., 2015. Water contact angles on quartz surfaces under supercritical CO2 sequestration conditions: Experimental and molecular dynamics simulation studies. Int. J. Greenh. Gas Control. 42, 655–665.

Delenne, J.-Y., Richefeu, V., Radjai, F., 2015. Liquid clustering and capillary pressure in granular media. J. Fluid Mech. 762, R5.

Fakhari, A., Li, Y., Bolster, D., Christensen, K.T., 2018. A phase-field lattice Boltzmann model for simulating multiphase flows in porous media: Application and comparison to experiments of CO2 sequestration at pore scale. Adv. Water Resour. 114, 119–134.

Galindo-Torres, S., Scheuermann, A., Li, L., 2016. Boundary effects on the soil water characteristic curves obtained from lattice Boltzmann simulations. Comput. Geotech. 71, 136–146.

Ginzbourg, I., Adler, P., 1994. Boundary flow condition analysis for the three-dimensional lattice Boltzmann model. J. de Phys. II 4 (2), 191–214.

He, X., Chen, S., Zhang, R., 1999. A Lattice Boltzmann scheme for incompressible multiphase flow and its application in simulation of Rayleigh–Taylor instability. J. Comput. Phys. 152 (2), 642–663. http://dx.doi.org/10.1006/jcph.1999.6257.

He, Q., Li, Y., Huang, W., Hu, Y., Wang, Y., 2019. Phase-field-based lattice Boltzmann model for liquid-gas-solid flow. Phys. Rev. E 100 (3), 033314.

Hosseini, R., Kumar, K., 2025. Micromechanical evaluation of the effective stress parameter using the multiphase lattice Boltzmann method and investigation of its hysteresis. Comput. Geotech. 188, 107564.

Hosseini, R., Kumar, K., Delenne, J.-Y., 2024. Investigating the source of hysteresis in the soil–water characteristic curve using the multiphase lattice Boltzmann method. Acta Geotech. 1–25.

Hu, Y., Li, D., He, Q., 2020. Generalized conservative phase field model and its lattice Boltzmann scheme for multicomponent multiphase flows. Int. J. Multiph. Flow 132, 103432.

Huang, H., Krafczyk, M., Lu, X., 2011. Forcing term in single-phase and Shan-Chen-type multiphase lattice Boltzmann models. Phys. Rev. E—Statistical, Nonlinear, Soft Matter Phys. 84 (4), 046710.

Huang, H., Sukop, M., Lu, X., 2015. Multiphase Lattice Boltzmann Methods: Theory and Application. John Wiley & Sons.

Huang, H., Thorne Jr., D.T., Schaap, M.G., Sukop, M.C., 2007. Proposed approximation for contact angles in shan-and-chen-type multicomponent multiphase lattice Boltzmann models. Phys. Rev. E 76 (6), 066701.

Jansen, H.P., Sotthewes, K., van Swigchem, J., Zandvliet, H.J., Kooij, E.S., 2013. Lattice Boltzmann modeling of directional wetting: Comparing simulations to experiments. Phys. Rev. E 88 (1), 013008.

Khajepor, S., Cui, J., Dewar, M., Chen, B., 2019. A study of wall boundary conditions in pseudopotential lattice Boltzmann models. Comput. & Fluids 193, 103896.

Kido, R., Ueda, H., 2025. Infiltration characteristics of bentonite-based stabilizing fluid into pore spaces of sand investigated by X-ray micro-CT analysis. Acta Geotech. 1–20.

Krüger, T., 2017. The Lattice Boltzmann method. In: Graduate texts in physics, Springer International Publishing, ISBN: 978-3-319-44647-9, http://dx.doi.org/10.1007/978-3-319-44649-3.

Li, Z., Galindo-Torres, S., Yan, G., Scheuermann, A., Li, L., 2018. A lattice Boltzmann investigation of steady-state fluid distribution, capillary pressure and relative permeability of a porous medium: Effects of fluid and geometrical properties. Adv. Water Resour. 116, 153–166.

Liu, H., Kang, Q., Leonardi, C.R., Schmieschek, S., Narváez, A., Jones, B.D., Williams, J.R., Valocchi, A.J., Harting, J., 2016. Multiphase lattice Boltzmann simulations for porous media applications. Comput. Geosci. 20 (4), 777–805. http://dx.doi.org/10.1007/s10596-015-9542-3.

Liu, H., Zhang, Y., Valocchi, A.J., 2015. Lattice Boltzmann simulation of immiscible fluid displacement in porous media: Homogeneous versus heterogeneous pore network. Phys. Fluids 27 (5), 052103. http://dx.doi.org/10.1063/1.4921611.

Luo, L.-S., Liao, W., Chen, X., Peng, Y., Zhang, W., 2011. Numerics of the lattice Boltzmann method: Effects of collision models on the lattice Boltzmann simulations. Phys. Rev. E 83 (5), 056710. http://dx.doi.org/10.1103/PhysRevE.83.056710, URL: https://link.aps.org/doi/10.1103/PhysRevE.83.056710 Publisher: American Physical Society.

Martys, N.S., Chen, H., 1996. Simulation of multicomponent fluids in complex three-dimensional geometries by the lattice Boltzmann method. Phys. Rev. E 53 (1), 743–750. http://dx.doi.org/10.1103/PhysRevE.53.743, Publisher: American Physical Society.

Milatz, M., Andò, E., Viggiani, G.C., Mora, S., 2022. In situ X-ray CT imaging of transient water retention experiments with cyclic drainage and imbibition. Open Geomech. 3, 1–33.

Montellà, E., Chareyre, B., Salager, S., Gens, A., 2020. Benchmark cases for a multi-component lattice–Boltzmann method in hydrostatic conditions. MethodsX 7, 101090.

Nekoeian, S., Goharrizi, A.S., Jamialahmadi, M., Jafari, S., Sotoudeh, F., 2018. A novel shan and chen type lattice Boltzmann two phase method to study the capillary pressure curves of an oil water pair in a porous media. Petroleum 4 (3), 347–357.

Pan, C., Hilpert, M., Miller, C., 2004. Lattice-Boltzmann simulation of two-phase flow in porous media. Water Resour. Res. 40 (1).

Qian, Y.-H., d'Humières, D., Lallemand, P., 1992. Lattice BGK models for Navier-Stokes equation. Europhys. Lett. 17 (6), 479.

Schaap, M.G., Porter, M.L., Christensen, B.S., Wildenschild, D., 2007. Comparison of pressure-saturation characteristics derived from computed tomography and lattice Boltzmann simulations. Water Resour. Res. 43 (12).

Shan, X., Chen, H., 1993. Lattice Boltzmann model for simulating flows with multiple phases and components. Phys. Rev. E 47 (3), 1815–1819. http://dx.doi.org/10.1103/PhysRevE.47.1815.

Shan, X., Doolen, G., 1995. Multicomponent lattice-Boltzmann model with interparticle interaction. J. Stat. Phys. 81 (1), 379–393. http://dx.doi.org/10.1007/BF02179985.

Sukop, M.C., Huang, H., Lin, C.L., Deo, M.D., Oh, K., Miller, J.D., 2008. Distribution of multiphase fluids in porous media: Comparison between lattice Boltzmann modeling and micro-x-ray tomography. Phys. Rev. E—Statistical, Nonlinear, Soft Matter Phys. 77 (2), 026710.

Sukop, M.C., Or, D., 2004. Lattice Boltzmann method for modeling liquid-vapor interface configurations in porous media. Water Resour. Res. 40 (1).

Sukop, M., Thorne, D., 2005. Lattice Boltzmann modeling: an introduction for geoscientists and engineers, 2005. In: Google Scholar Google Scholar Digital Library Digital Library. DOI.

Van Genuchten, M.T., 1980. A closed-form equation for predicting the hydraulic conductivity of unsaturated soils. Soil Sci. Am. J. 44 (5), 892–898.

Wang, Q., Milatz, M., Hosseini, R., Kumar, K., 2023. Multiphase lattice Boltzmann modeling of cyclic water retention behavior in unsaturated sand based on X-ray computed tomography. Can. Geotech. J. 60 (9), 1429–1446.

Wang, L., Peng, Z.-R., 2020. Pressure boundary condition in a multiphase lattice Boltzmann method and its applications on simulations of two-phase flows. Internat. J. Numer. Methods Fluids 92 (7), 669–686.

Yang, J., Boek, E.S., 2013. A comparison study of multi-component Lattice Boltzmann models for flow in porous media applications. Mesoscopic Methods in Engineering and Science, Comput. Math. Appl. Mesoscopic Methods in Engineering and Science, 65 (6), 882–890.http://dx.doi.org/10.1016/j.camwa.2012.11.022,

Ye, F., Di, Q., Wang, W., Chen, F., Chen, H., Hua, S., 2018. Comparative study of two lattice Boltzmann multiphase models for simulating wetting phenomena: implementing static contact angles based on the geometric formulation. Appl. Math. Mech. 39 (4), 513–528. http://dx.doi.org/10.1007/s10483-018-2320-7, URL: http://link.springer.com/10.1007/s10483-018-2320-7.

Yiotis, A.G., Psihogios, J., Kainourgiakis, M.E., Papaioannou, A., Stubos, A.K., 2007. A lattice Boltzmann study of viscous coupling effects in immiscible two-phase flow in porous media. Colloids Surfaces A: Physicochem. Eng. Asp. 300 (1–2), 35–49.

Younes, N., Benseghier, Z., Millet, O., Wautier, A., Nicot, F., Wan, R., 2022. Phase-field lattice Boltzmann model for liquid bridges and coalescence in wet granular media. Powder Technol. 411, 117942.

Younes, N., Wautier, A., Wan, R., Millet, O., Nicot, F., Bouchard, R., 2023. DEM-lbm coupling for partially saturated granular assemblies. Comput. Geotech. 162, 105677.

Yuan, P., Schaefer, L., 2006. Equations of state in a lattice Boltzmann model. Phys. Fluids 18 (4).

Yuana, K.A., Jalaali, B., Budiana, E.P., Widyaparaga, A., et al., 2021. Lattice Boltzmann simulation of the Rayleigh–taylor instability (RTI) during the mixing of the immiscible fluids. Eur. J. Mech. B Fluids 85, 276–288.

Zhang, R., He, X., Chen, S., 2000. Interface and surface tension in incompressible lattice Boltzmann multiphase model. Comput. Phys. Comm. 129 (1–3), 121–130.

Zhang, S., Li, J., Wang, T., Zhu, Q., Wu, K., Chen, Z., Chen, Z., 2024. Modeling of immiscible fluid flow in mixed-wetted porous media using the lattice Boltzmann method. In: ARMA US Rock Mechanics/Geomechanics Symposium. ARMA, D022S024R001.

Zhao, X., Sang, Q., Ma, J., Sarma, H., Dong, M., 2021. Method of determining the cohesion and adhesion parameters in the Shan-Chen multicomponent multiphase lattice Boltzmann models. Comput. & Fluids 222, 104925. http://dx.doi.org/10.1016/j.compfluid.2021.104925.

Zhou, X., Xu, Z., Xia, Y., Li, B., Qin, J., 2020. Pore-scale investigation on reactive flow in porous media with immiscible phase using lattice Boltzmann method. J. Pet. Sci. Eng. 191, 107224. http://dx.doi.org/10.1016/j.petrol.2020.107224.

Zhu, J., Dai, Z., Wang, Z., Chu, S., Wang, M., 2024. Investigation on enhanced density ratio recovery and numerical stability in real physical field under multi-component multiphase LBM. Int. Commun. Heat Mass Transfer 156, 107673.

Zou, Q., He, X., 1997. On pressure and velocity boundary conditions for the lattice Boltzmann BGK model. Phys. Fluids 9 (6), 1591–1598.